Morphological and Doppler UHR-OCT Imaging of Retinal Degeneration Induced by Sodium Iodate Toxicity in a Rat Model

by

Man Chun Tam

A thesis
presented to the University of Waterloo
in fulfillment of the
thesis requirement for the degree of
Master of Science
in
Physics

Waterloo, Ontario, Canada, 2014

© Man Chun Tam 2014

AUTHOR'S DECLARATION

I hereby declare that I am the sole author of this thesis except where explicitly noted. This is a true copy of the thesis, including any required final revisions, as accepted by my examiners.

I understand that my thesis may be made electronically available to the public.

Abstract

A high speed, high resolution spectral domain optical coherence tomography (SD-OCT) system was used to study *in*-vivo early morphological changes and optical nerve head (ONH) blood flow in the Long Evans rat retina, induced by administration of sodium iodate ($NaIO_3$). Linear and circular scanned OCT images were acquired at the same location in the retina from healthy control rats and from rats injected with 40mg/kg of $NaIO_3$ solution at 1, 3, 6 12, 24, 72 and 168 hours post drug administration. Morphological OCT images showed changes in the optical reflectance and layer thickness of the photoreceptor IS and OS. The formation of a new low reflective layer between the photoreceptor OS and the RPE was observed in all tested rats. This new layer appeared as early as 1 hour, increased in thickness after 6 hours, and disappeared by 12 hours post $NaIO_3$ injection. The low optical reflectance and the dynamics of this new layer suggest that it was most likely fluid accumulation. Comparison with H&E stained histological sections and IgG immunohistochemistry revealed minimal photoreceptor OS cell swelling at hour 1, detachment of the OS from the RPE by hour 3, and breaking of the blood-retina barrier with significant fluid accumulation by hour 6 post $NaIO_3$ injection. The Doppler Optical Micro-Angiography (DOMAG) algorithm was used to carry out quantitative analysis of the ONH blood flow. Estimation of flow rate on each ONH vessel was done by measurements of the Doppler angle, vessel size and the axial velocity. This study has demonstrated that the capability of UHR-OCT to study optical reflectance and layer thickness changes, rearrangement and detachment of the photoreceptor OS and RPE layers, together with flow rate estimation of retinal blood vessels. Therefore, it can serve as markers in future non-invasive, in-vivo studies of disease or drug induced retinal degeneration in ophthalmic research.

Acknowledgements

I would like to thank

My supervisor, Dr. Kostakinda Bizheva, for her continuous guidance during my MSc project;

My committee members and examiners, Dr. Donna Strickland, Dr. Natalie Hutchings, Dr. Kevin Resch and Dr. Zoya Leonenko for all of their support and constructive discussions;

Nancy Gibson, Martin Ryan and Jean Flanagan, for all their help and advices in animal handling;

Dr. Azhar Zam, for his help in building my MATLAB code in OCT data processing;

Dr. Alireza Akhlagh Moayed and Dr. Sepideh Hariri, for their teachings about OCT imaging on animals;

Dr. Denise Hileeto for her assistance in histology;

Daryl Chulho Hyun, for his LabVIEW code used for the operation of our SD-OCT system;

Kruno Dworski and Herman van der Heide from the Science Shop for building supportive electrical and mechanical components for the SD-OCT system;

I also would like to specially thank

Dr. Sebastian Marschall, for being a great and knowledgeable colleague who teaches me a lot not only in LabVIEW programming but also in OCT data processing and paper writing;

All my colleagues: Bruce Calvert, Michal Vymyslicky, David Donghyun Lee, Bingyao Tan, Kirstie Carter and Kevin Si, not only for their full assistance with imaging and data processing but also for every day they spent with me in the biomedical imaging lab for the past 2 years.

Dedication

To my family. Have a good one!

Table of Contents

List of Abbreviations

OCT	Optical Coherence Tomography
UHROCT	Ultra-High Resolution Optical Coherence Tomography
TD-OCT	Time Domain Optical Coherence Tomography
FD-OCT	Fourier Domain Optical Coherence Tomography
SD-OCT	Spectral Domain Optical Coherence Tomography
SS-OCT	Swept Source Optical Coherence Tomography
DOCT	Doppler Optical Coherence Tomography
FOCT	Functional Optical Coherence Tomography
OMAG	Optical Micro-Angiography
DOMAG	Doppler Optical Micro-Angiography
MRI	Magnetic Resonance Imaging
NIR	Near-Infrared
IFT	Inverse Fourier Transform
FWHM	Full Width Half Maximum
NA	Numerical Aperture
PSF	Point Spread Function
SNR	Signal to Noise Ratio
AMD	Age-Related Macular Degeneration
RP	Retinitis Pigmentosa
CGA	Central Geographic Atrophy
CNV	Choroidal Neovascular
$NaIO_3$	Sodium Iodate
CC	Choroidal Capillaries
CSI	Chorio-scleral Interface
ONH	Optical Nerve Head
ERG	Electroretinography
IOS	Intrinsic Optical Signal
SLD	SuperluminescentDiode
PC	Polarization Controllers

CL	Collimating Lens
FL	Focusing Lens
DC	Dispersion Compensation Unit
M	Mirror
TS	Translation Stage
DG	Diffraction Grating
CCD	Charge Coupled Device
FOV	Field of View
NFL	Nerve Fiber Layer
GCL	Ganglion Cell Layer
IPL	Inner Plexiform Layer
INL	Inner Nuclear Layer
ONL	Outer Nuclear Layer
ELM	External Limiting Membrane
PR	Photoreceptor
IS	Inner Segment of Photoreceptors
OS	Outer Segment of Photoreceptors
RPE	Retina Pigment Epithelium
C	Choroid
S	Sclera

List of Figures

List of Tables

Chapter 1

Overview and Motivation

1.1 OCT used in *In Vivo* Retina Imaging and Animal Disease Model

Over the past few decades, medical imaging has played an essential role in monitoring humans' health by studying the morphology of biological tissues in various organs. There are numerous types of medical imaging techniques: magnetic resonance imaging (MRI), Positron Emission Tomography (PET), X-ray imaging, ultrasound imaging, confocal microscopy…just to mention a few. Those methods are capable of virtual reconstruction of the morphology of biological tissue from the macroscopic scale (i.e. bones, organs, muscles) to the microscopic scale (micro-capillaries, cells). Most of these methods share another very important characteristic: they are capable of *in vivo*, non-invasive imaging of the tissue morphology.

Optical coherence tomography (OCT) is an imaging technique invented in the early 1990s [1], [2]. The principle of operation of OCT is very similar to ultrasound, though instead of longitudinal sound waves, OCT uses transverse optical (electromagnetic) waves to scan the sample and detect the backscattered signal from various tissue sites or layers from different imaging depths. OCT is based on low-coherence interferometry. A typical OCT system uses near-infrared as light source and the light is separated into two arms – a sample arm containing the subject to be imaged and a reference arm which is usually a mirror. Recombination of the reflected light from the sample and reference arm results in an interferogram which contains sample information. In terms of spatial resolution and imaging depth, OCT fills the gap between imaging technologies such as ultrasound tomography and confocal microscopy. Amongst different organs, retina perhaps is the best illustration of the amazing capability of three-dimensional morphological reconstruction of OCT technology. OCT is currently the leading technology for ophthalmic diagnostics in clinics, as well as one of the most successful research tool used for investigating animal models of retinal diseases [3]-[11].

Animal models are widely used in biomedical research to simulate human disease development which may provide useful information as to the origins and pathways of the disease progression. Rodents are the most common disease model subjects for the following reasons: a)

rodents are mammals same as humans; b) rodents have fast metabolic rate, which means that any experimentally induced disease are developing within a much shorter time period, compared to the disease progression in humans which allows for carrying out longitudinal studies that cannot be easily conducted in human subjects; c) the breeding rate of rodents is high, and the cost of rodent housing is very low compared to the cost of other animal models, which makes rodents easily accessible and manageable for research studies. One of the well-known retinal disease models is the $NaIO_3$ model, which is used to simulate age macular degeneration (AMD) and retinitis pigmentosa (RP). OCT has been shown its ability to image structural and vascular changes in these retinal diseases.

This project describes the use of ultra-high resolution spectral domain OCT (SD-OCT) technology to investigate morphological and vascular changes in outer retina degeneration in the rat retina, induced by administration of sodium iodate ($NaIO_3$). Two variations of OCT techniques, called Doppler OCT (DOCT) and Optical Micro-Angiography (OMAG) are used in this study. DOCT measures the velocity of blood vessels, while OMAG helps to differentiate the perfusion in interest, which is optical nerve head (ONH) in this work, from other static tissues. These two methods are combined as Doppler micro-angiography (DOMAG) to observe and quantify vascular changes in the $NaIO_3$ treated rat retina.

1.2 Thesis Outline

Chapter 2 is an overview of general concepts and features of OCT. These include Michelson-interferometry, axial and transverse resolution, spectral domain OCT, sensitivity and scanning range, dispersion compensation, DOCT with focus on phase-resolved method and OMAG with focus on digital frequency ramping method (DFRM).

Chapter 3 provides some background of how the $NaIO_3$ toxicity causes retinal degeneration, specifically in the retinal pigment epithelium (RPE) layer. Questions are addressed if such toxicity can also affect the perfusion in retina, which might be possible to be examined through DOMAG.

Chapter 4 describes the SD-OCT system used to image the retina of $NaIO_3$ injected rats. Design of imaging probe, animal handling and preparation, imaging protocols, acquisition and processing, are discussed in detail.

Chapter 5 discusses the results from this study related to morphological changes in the rat retina induced by$NaIO_3$ toxicity. The retinal degeneration is examined as a function of time by comparing morphological OCT images of the $NaIO_3$ treated rat retina, acquired at different post-injection time points. Then it analyzes the effect of $NaIO_3$ toxicity on the optic nerve head (ONH) blood flow in rats. The perfusion changes in ONH at different post-injection time points are compared in color DOMAG images. The axial velocity, Doppler angle, absolute velocity and flow rate of every ONH artery and vein are calculated. Problems encountered in terms of precision and reliability of Doppler angle and flow rate are discussed.

Appendix A demonstrates DOCT's reliability of quantitatively analyzing fluid flow. The manuscript describes a phantom flow system using titanium dioxide (TiO_2) solution as the fluid and the flow was imaged by the SD-OCT system. The flow rate estimated by the DOCT algorithm is compared to its expected value and the result is discussed.

Chapter 2

Optical Coherence Tomography (OCT)

2.1 OCT Fundamentals

2.1.1 Principle of Operation

Optical Coherence Tomography (OCT), is an optical imaging technique first demonstrated by Huang et al. in 1991 [2], which allows for *in vivo*, non-invasive, high resolution three dimensional imaging of biological tissue [1]. The principle of operation of OCT is based on Michelson-interferometry, in which the imaging beam from a light source is divided by a beam splitter into two optical beams directed at different paths: reference arm and sample arm. A schematic of a typical Michelson-interferometer is shown in Fig. 2.1. The imaging sample is placed at the end of the sample arm, while a mirror is placed at the end of the reference arm and both objects are illuminated with optical beams generated by the light source. In the detector arm, the back scattered light from the sample combines with the reflected reference beam to form an interference pattern, the envelope of which provides a measure of the amount of reflected light as a function of distance in the sample arm of the interferometer. This graph is also commonly referred as an A-scan, in which the intensity tells the reflectance of the sample at different depths. By introducing a pair of galvanometric mirrors in the sample arm, the sample beam can be directed to different positions of the sample. By moving one of the galvanometric mirrors, the beam can do repetitive A-scans along a transverse direction, which is also called a B-scan; working together with another mirror the beam can be directed to both transverse directions. Repetitive B-scans form a three-dimensional stack of images which resembles the morphological profile of the whole sample.

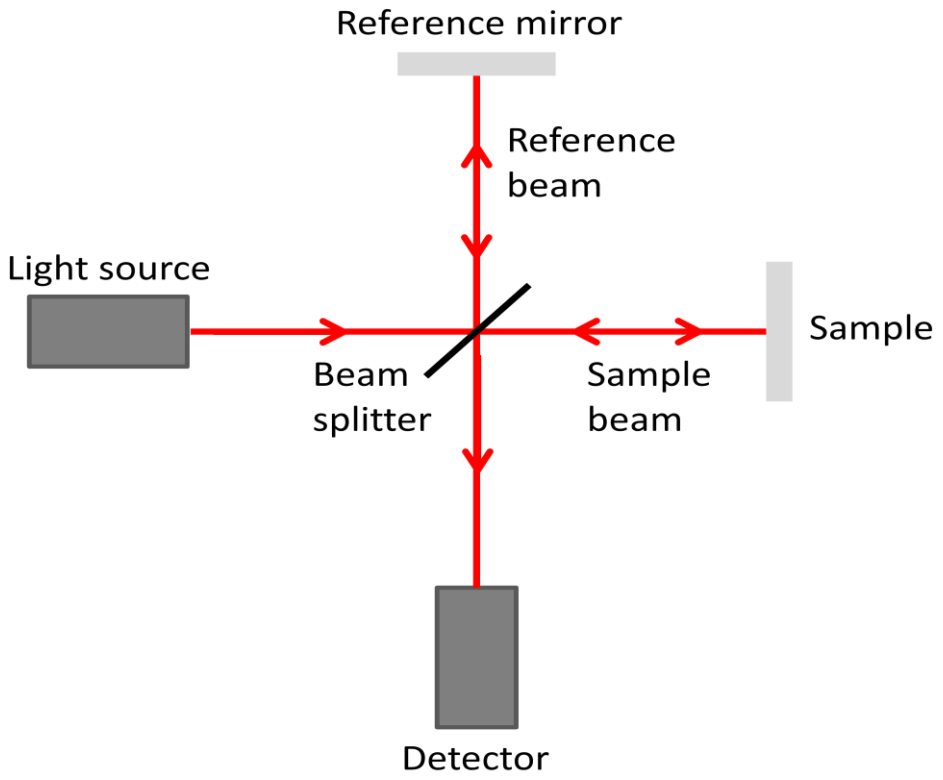

Fig. 2.1 Schematic diagram of a typical Michelson-interferometer.

To start with, assuming there is a sample with only one reflective layer. In an A-scan, the electric field $\mathbf{E}_{\text{total}}$ in the detector arm is the superposition of the reference and sample light waves, $\mathbf{E}_r$ and $\mathbf{E}_s$:

$$\mathbf{E}_{\text{total}} = \mathbf{E}_r + \mathbf{E}_s \tag{2.1}$$

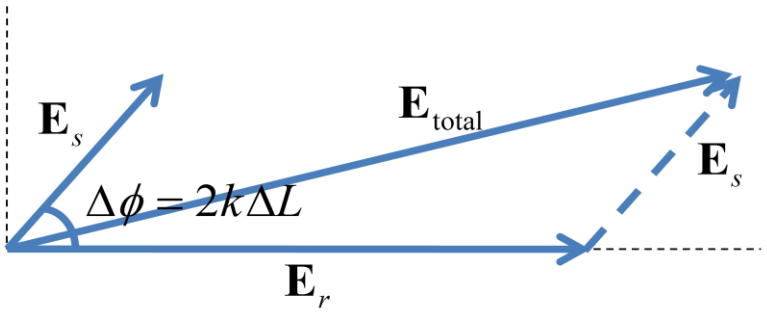

Fig. 2.2 A simple phase diagram representation of the sum of the electric fields in reference and sample arm.

As shown in Fig. 2.2, when there is a path length difference ΔL between the reference and sample arms, the phase difference between is $\Delta\phi = 2k\Delta L$, where the factor of 2 accounts for the light travels forth and back by reflection or backscattering in the two arms. The intensity in the detector arm I which is proportional to the square of $\mathbf{E}_{\text{total}}$, can be obtained by using simple trigonometry:

$$I \sim E_r^2 + E_s^2 + 2E_r E_s \cos(2k\Delta L) \tag{2.2}$$

where k is the wavenumber of the light source. While the first and second terms in Eq. (2.2) are just constants, the third cosine term contributes the interference signal and plays a dominant role in OCT image processing. E_s, the magnitude of the backscattered light from the imaged object, which in the case of biological tissue is very weak. However, benefited from the Michelson-interferometry configuration, E_s can multiply itself with the reference light E_r, then the signal can be strongly amplified and becomes detectable.

2.1.2 OCT Resolution

The interference pattern is formed only when the path difference between the sample and reference arm is no more than the coherence length l_c, which describes the propagation distance of the light maintaining a specified degree of coherence. Assuming the light source has a Gaussian spectrum

$$S(\omega) = S_0 \left(\frac{1}{2}\right)^{\frac{\omega^2}{\Delta\omega^2/4}} = S_0 e^{-\frac{\omega^2 \ln 2}{\Delta\omega^2/4}} \tag{2.3}$$

where $\Delta\omega$ is the full-width-half maximum (FWHM) of $S(\omega)$. The point spread function (PSF), which is the Fourier transform of the spectrum, is also Gaussian in shape:

$$\mathrm{I}(\tau) = \int_{-\infty}^{\infty} S(\omega)\, \mathrm{e}^{i\omega\tau}\, d\omega = I_0 \left(\frac{1}{2}\right)^{\frac{\tau^2}{\Delta\tau^2/4}} = I_0 e^{-\frac{\tau^2 \ln 2}{\Delta\tau^2/4}} \tag{2.4}$$

where $\Delta\tau$ is the FWHM of $\mathrm{I}(\tau)$. It can be shown that $\Delta\omega$ and $\Delta\tau$ have an inverse proportionality relationship:

$$\Delta\tau = \frac{8\ln 2}{\Delta\omega} \tag{2.5}$$

By converting the time domain into spatial domain, $l_c = c\Delta\tau / n$, where n is the refractive index of the sample, in which the coherence length is actually the FWHM in the spatial domain. In addition, we can also express $\Delta\omega$ in terms of the central wavelength of the light source λ_0 and the FWHM of wavelength $\Delta\lambda$, where $\Delta\omega = \frac{2\pi c\Delta\lambda}{\lambda_0^2}$. By rewriting Eq. (2.5), the axial resolution Δz along the imaging depth of a sample, which is also half of the coherence length, is [1], [3]

$$\Delta z = \frac{l_c}{2} = \frac{2\ln 2}{n\pi}\frac{\lambda_0^2}{\Delta\lambda} \tag{2.6}$$

Since Δz and l_c are inversely proportional to $\Delta\lambda$, as a result, a light source with broader bandwidth gives a better axial resolution but shorter total imaging depth [1].

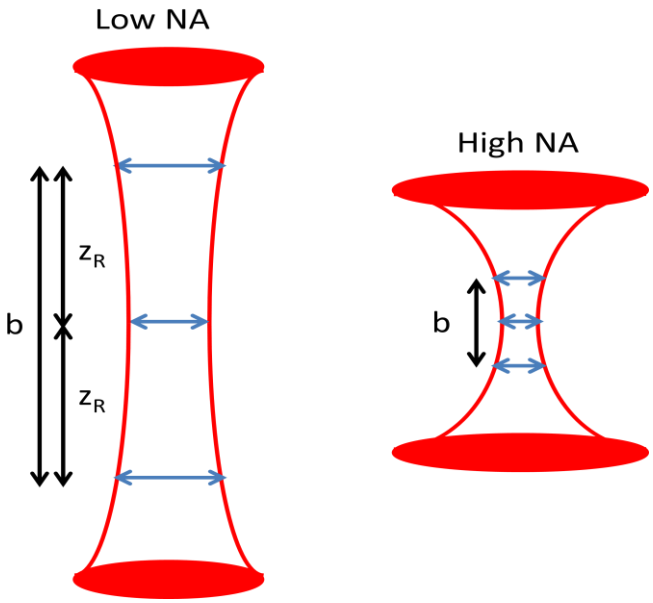

Fig. 2.3 The relation between depth of focus and transverse resolution for Gaussian beam with high and low NA.

While the axial resolution depends only on the light source and the optical properties of the sample, the lateral or transverse resolution also depends on the choice of imaging lens in the sample arm (Refer to Fig. 2.3). For a Gaussian beam, the OCT transverse resolution is defined by the radius of the spot size (Airy disk) of the focused beam on the sample [1]:

$$\Delta x = \frac{4\lambda_0}{n\pi}\frac{f}{d} = \frac{0.61}{n}\frac{\lambda_0}{NA} \tag{2.7}$$

where f is the focal length, d is the beam diameter of the optical beam on the imaging lens and NA is the numerical aperture of the beam. The transverse resolution is also related to the depth of focus or the confocal parameter b, which is also two times of the Rayleigh range z_R, and can be expressed as

$$b = 2z_R = \frac{\pi \Delta x^2}{n\lambda} \tag{2.8}$$

From Eqs. (2.7) and (2.8), a larger the *NA* results in a better transverse resolution but smaller depth of focus.

2.1.3 Spectral Domain OCT

During the early years of OCT development, in order to obtain imaging profiles for the whole axial depth range of a biological tissue, the reference arm mirror had to move back and forth in order to match the path lengths of different axial positions in the sample. This method is also known as Time-Domain OCT (TD-OCT) [1], [3]. Since a mechanical device is required to adjust the position of the reference mirror along the whole axial range, and the scanning rates of galvanometric scanners are limited to only a few kHz, 2D and 3D imaging with TD-OCT is time consuming. A more advanced version of OCT technology, that does not utilize mechanical scanning along the imaging depth, called Fourier domain OCT (FD-OCT) [1], [3] was invented. In FD-OCT the reference mirror is fixed and a broadband light source is used. Light reflected from different positions within the imaged object interferes with the strong reflection from the reference mirror to generate an interference pattern at the detector. By applying Fourier Transform to the spectrum, the reflectance profile of the imaged object as a function of imaging depth is recorded. Since the reference mirror in FD-OCT is stationary, the image acquisition speed in FD-OCT is much faster than that of TD-OCT.

There are two different types of FD-OCT technologies: Spectral Domain OCT (SD-OCT) and Swept Source OCT (SS-OCT). In SD-OCT, a broadband light source is used as the input and a combination of a high resolution spectrometer and a linear array camera is used as the detector

end of the OCT system. In SS-OCT a frequency-swept laser is used as the light source and a single photodiode is used to detect the signal as a function of time and frequency, which then is converted to a depth position in the imaged object.

Since the project described in this thesis was completed using a SD-OCT system, the following texts, equations and chapters are based on SD-OCT system. Consider a more extended, realistic version of Eq. (2.2). A biological tissue, which consists of many different reflective layers, is placed in the end of the sample arm. For an imaging light source with spectrum $S(\omega)$ and electric field $E(\omega)$, where $S(\omega) \propto E^2(\omega)$, assume the n^{th} layer has a path length difference ΔL_n and time delay τ_n with the reference mirror. Using the phasor addition method similar to the one shown in Fig. 2.2, the backscattered electric fields from the reference and sample arm can be expressed as complex numbers $\tilde{E}_{\text{reference}}(\omega)$ and $\tilde{E}_{\text{sample}}(\omega)$:

$$\begin{cases} \tilde{E}_{\text{reference}}(\omega) = \sqrt{a_r}E(\omega) \\ \tilde{E}_{\text{sample}}(\omega) = E(\omega)\sum_n \sqrt{a_n}e^{i\omega\tau_n} \end{cases} \tag{2.9}$$

where ω is the frequency of the light source, a_r and a_n are the attenuation coefficients of the backscattered light from the reference mirror and the n^{th} layer in the sample respectively. The resultant electric field is $\tilde{E}_{\text{total}}(\omega) = \tilde{E}_{\text{reference}}(\omega) + \tilde{E}_{\text{sample}}(\omega)$. Consider the square of its modulus,

$$\begin{aligned} \left|\tilde{E}_{\text{total}}(\omega)\right|^2 &= \left[E(\omega)\left(\sqrt{a_r} + \sum_n \sqrt{a_n}e^{i\omega\tau_n}\right)\right]\left[E^*(\omega)\left(\sqrt{a_r} + \sum_n \sqrt{a_n}e^{-i\omega\tau_n}\right)\right] \\ &= E^2(\omega)\left[a_r + \sum_n a_n + 2\sum_n \sqrt{a_r a_n}\cos(\omega\tau_n) + 2\sum_{m\neq n} \sqrt{a_n a_m}\cos(\omega\tau_{nm})\right] \end{aligned} \tag{2.10}$$

The detector signal $S_{\text{total}}(\omega)$ is then

$$S_{\text{total}}(\omega) = S(\omega)\left[a_r + \sum_n a_n + 2\sum_n \sqrt{a_r a_n}\cos(\omega\tau_n) + 2\sum_{m\neq n} \sqrt{a_n a_m}\cos(\omega\tau_{nm})\right] \tag{2.11}$$

where $\tau_{nm} = \tau_n - \tau_m$ is the time delay between the n^{th} and the m^{th} layer. By taking inverse Fourier transform, the structural profile of the sample along the axial direction can be obtained:

$$\begin{aligned}\tilde{I}(\tau) &= \mathrm{IFT}^{\omega\to\tau}\left\{S_{\mathrm{total}}(\omega)\right\} \\ &= \left(a_r + \sum_n a_n\right)\Gamma(\tau) + \sum_n \sqrt{a_r a_n}\left(\Gamma(\tau)\otimes\delta(\tau\pm\tau_n)\right) + \sum_{m\neq n}\sqrt{a_n a_m}\left(\Gamma(\tau)\otimes\delta(\tau\pm\tau_{nm})\right)\end{aligned} \tag{2.12}$$

where $\Gamma(\tau) = \mathrm{IFT}^{\omega\to\tau}\left\{S(\omega)\right\}$. The first and second terms are just DC signals from the reference mirror and all the layers in the sample; the third term is called the 'cross-correlation' term resulted from the interference between the reference mirror and the n^{th} layer; the fourth term is called the 'auto-correlation' term, also known as coherence noise, resulted from the interference between the n^{th} and the m^{th} layer of the sample itself. The cross-correlation term is the 'true' OCT signal that being mainly concerned, while the auto-correlation term is an unwanted artifact. By increasing the reference arm power to a level where $a_r >> a_n$, such artifact can become negligible compared with the cross-correlation term.

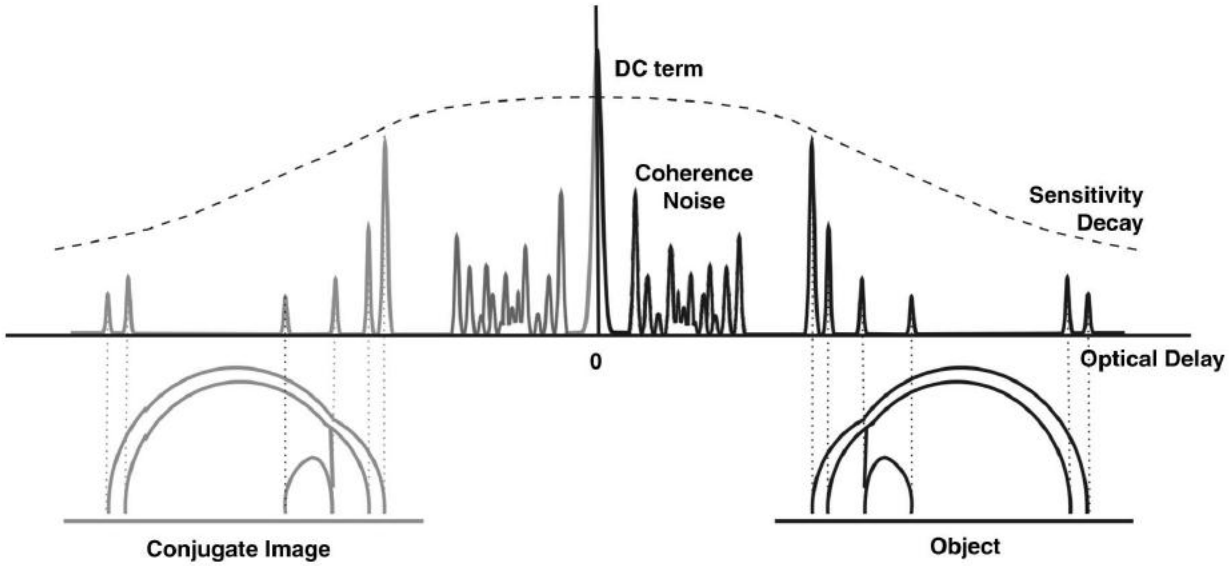

Fig. 2.4 Illustration of A-scan signal in SD-OCT. Besides the A-scan corresponding to the structure, the resultant signal also includes a conjugate symmetrical image and coherence noise terms. Additionally all signals are affected by the sensitivity drop-off caused by the limited spectral resolving power of OCT spectrometers. Figure adopted and reprinted from reference [3].

Fig. 2.4 illustrates an A-scan signal $\tilde{I}(\tau)$ from an eye. The cross-correlation term is represented by various peaks of PSF which correspond to different highly reflective layers in the eye. The smaller peaks are the auto-correlation artifacts, located close to the DC signal is at the middle of

the graph. Notice that due to the '±' sign in Eq. (2.12), there is a conjugate symmetrical image at the left of Fig. 2.3. Therefore for a CCD linear array consists of *N* pixels, only *N*/2 pixels are useful for the OCT signal in concern while another *N*/2 just form a mirror image.

2.1.4 Signal to Noise Ratio (SNR), Sensitivity and Maximum Scanning Range

The signal to noise ratio (SNR) in OCT system is defined as

$$SNR = \frac{\left\langle \tilde{I}(\tau) \right\rangle^2}{\sigma^2} \tag{2.13}$$

in which σ^2 is the variance of the noise. In TD-OCT it is

$$SNR_{TD-OCT} = \frac{\rho S_{TD-OCT} R_s}{2eB_{TD-OCT}} \tag{2.14}$$

where ρ is detector sensitivity, e is the electron charge, $S_{TD-OCT}R_s$ is the power returning from the sample and B_{TD-OCT} is the detection bandwidth of TD-OCT system. While in FD-OCT it is [1]

$$SNR_{FD-OCT} = \frac{\rho S_{FD-OCT} R_s}{2eB_{FD-OCT}} \frac{M}{2} \tag{2.15}$$

where $S_{FD-OCT}R_s$ is the power returning from the sample, B_{FD-OCT} is the detection bandwidth of FD-OCT system and M is the number of detector channels. In the case of a SD-OCT system, M is the number of pixels in the CCD camera. The 1/2 factor is attributed to the conjugate symmetrical image, in which only half of the pixels are used to produce the wanted OCT signal. In the case of the uniform spectrum where the intensity is the same for all detectable frequencies in the CCD window,

$$SNR_{FD-OCT} = SNR_{TD-OCT} \frac{M}{2} \tag{2.16}$$

Therefore the SNR in a FD-OCT is significantly larger than a TD-OCT system. Even in the case of Gaussian spectrum where SNR_{FD-OCT} is reduced by a factor of 2, it is still much larger than that of TD-OCT.

In practice, there is a sensitivity fall-off as the imaging depth increases (illustrated by the dash-curve in Fig. 2.3), which is attributed to the limitation of the spectral resolution in the detector, say, the CCD camera pixel spacing in SD-OCT. This fall-off can be modeled by convolving the detected interferogram $I_D(k)$ with a Gaussian function of FWHM $\delta_r k^2$:

$$I_D(k) \otimes \exp\left[-\frac{4\ln(2)k^2}{\delta_r k^2}\right] \overset{\text{FFT}}{\leftrightarrow} i_D(\hat{z}) \bullet \exp\left[-\frac{\hat{z}^2 \delta_r k^2}{4\ln(2)}\right] \tag{2.17}$$

From this model, the depth with a sensitivity falls off by a factor of 1/2 or 6 dB is

$$\hat{z}_{6\text{dB}} = \frac{2\ln 2}{\delta_r k} = \frac{\ln 2}{\pi} \frac{\lambda_0^2}{\delta_r \lambda} \tag{2.18}$$

According to Nyquist's theorem, the relation between sampling frequency interval $\delta_s \nu$ and sampling time interval $\delta_s t$ in a detector linear array with *M* pixels is

$$\delta_s \nu \delta_s t = \frac{1}{M} \tag{2.19}$$

which can also be expressed as sampling wavenumber interval $\delta_s k = 2\pi \delta_s \nu / c$ and sampling depth interval $\delta_s z = c\delta_s t / 2$ (the 1/2 factor here is attributed to the light path travelling forth and backscattered in the sample arm):

$$\delta_s z \delta_s k = \frac{\pi}{M} \tag{2.20}$$

Therefore the maximum imaging depth $z_{\max} = \frac{M \delta_s z}{2}$ (the 1/2 factor here is attributed to the conjugate symmetrical image) can be expressed as

$$z_{\max} = \frac{M \delta_s z}{2} = \frac{\pi}{2\delta_s k} = \frac{\lambda_0^2}{4\delta_s \lambda} \tag{2.21}$$

To conclude, SD-OCT is more advanced than TD-OCT in terms of much faster image acquisition time and better SNR. However, SD-OCT still has some drawbacks. It requires a CCD

camera as the detector, which is usually more expensive than the case of TD-OCT where only a photodiode is needed. In addition, SD-OCT has its reference mirror fixed which limits the maximum imaging depth, while TD-OCT has a movable reference mirror to provide a longer imaging depth.

2.1.5 Dispersion Mismatch and Compensation

Electromagnetic waves entering from air to a medium (e.g. glass, water, transparent biological tissue) would have the wavelength shortened as well as experience a phase change. In a typical OCT system, the sample arm consists of several lenses to focus or adjust size of the imaging beam at the surface of the imaged object, while the sample (e.g. eye, finger nail) consists of many layers with various thicknesses and refractive indices. Moreover, the reference and sample arms are not 'straight' in real situation; to increase flexibility for optical alignment, optical fibers are used in both arms and additional lenses are located at the output of those fibers to collimate the light. Those optical components are made of materials with refractive indices typically between 1 and 2.5. In most situations, the thicknesses and refractive indices of the optical materials in the reference and the sample arms of the OCT system are not exactly the same, which would cause a frequency dependent phase difference between them. This phenomenon is also known as dispersion mismatch. It causes broadening and asymmetry of the PSF and degrades the axial resolution. As a result, a blurred OCT image is produced.

Therefore dispersion compensation must be done in order to retrieve a high resolution image, which can be done both in 'physical' and 'numerical' way. For physical dispersion compensation, glass slides or cylinders (for example BK7 glass rods or prisms) can be introduced in the reference arm of the OCT system, to match the dispersion from the optical components in the sample arm of the system. To dispersion compensate the water in the biological tissue sample, water cells are put in the reference arm. By adjusting the thicknesses and refractive indices of those glasses or water cells to some suitable values, the sharpness of the PSF can be optimized and dispersion can be matched in certain extent. Since those glass pieces in the reference arm usually do not have exactly same thicknesses and refractive indices as the lenses in the sample arm, the physical method cannot perfectly perform the dispersion compensation. Therefore numerical compensation can be used to compensate the residual dispersion mismatch.

The numerical dispersion compensation method described below is mostly adopted from the work of Wojtkowski et al. in reference [12]. Recall Eq. (2.11), assume the auto-correlation term is negligible and the two DC terms are not in concern. When there is a dispersion mismatch, the equation can be rewritten as

$$S_{\text{total}}(\omega) = 2S(\omega)\sum_{n}\sqrt{a_r a_n}\cos\left[\omega\tau_n + \phi(\omega,\tau_n)\right] \tag{2.22}$$

where $\phi(\omega,\tau_n)$ is the phase mismatch between the reference arm and the n^{th} layer in the sample arm. For simplicity, take the complex form of the spectrum by Hilbert transform and consider the phase mismatch term outside the summation sign as a single term $\Phi(\omega)$, which depends on frequency only:

$$\tilde{S}_{\text{total}}(\omega) = \left|\tilde{S}_{\text{total}}(\omega)\right|\exp\left[i\Phi(\omega)\right] \tag{2.23}$$

To eliminate $\Phi(\omega)$, it is necessary to make up a model to simulate how it varies with ω. For the propagation constant $\beta(\omega)$ in any kind of material, it can be expanded as Taylor series:

$$\beta(\omega) = \beta(\omega_0) + \left.\frac{d\beta}{d\omega}\right|_{\omega_0}(\omega-\omega_0) + \frac{1}{2}\left.\frac{d^2\beta}{d\omega^2}\right|_{\omega_0}(\omega-\omega_0)^2 + \frac{1}{6}\left.\frac{d^3\beta}{d\omega^3}\right|_{\omega_0}(\omega-\omega_0)^3 + \cdots \tag{2.24}$$

The constant term $\beta(\omega_0)$ is the propagation constant at the center frequency ω_0 of the spectral bandwidth, while the second term $\left.\frac{d\beta}{d\omega}\right|_{\omega_0}$ is the inverse group velocity. The third term $\frac{1}{2}\left.\frac{d^2\beta}{d\omega^2}\right|_{\omega_0}$ describes the group velocity dispersion or a variation in group velocity with frequency. This is the leading order term that produces pulse broadening in femtosecond optics and broadening of the axial resolution in OCT. The fourth term $\frac{1}{6}\left.\frac{d^3\beta}{d\omega^3}\right|_{\omega_0}$ has been referred to as third-order dispersion, which produces asymmetric pulse distortion in femtosecond optics and asymmetric distortion of the point spread function in OCT. Higher order terms may also be present.

It is reasonable that $\Phi(\omega)$ also takes such polynomial form as $\beta(\omega_0)$. Since it is not useful to include a constant term for dispersion compensation and not physically reasonable to

change the group velocity, the 0^{th} and 1^{st} order terms can be neglected, hence only 2^{nd} and 3^{rd} order terms are considered:

$$\Phi(\omega) = a_2(\omega - \omega_0)^2 + a_3(\omega - \omega_0)^3 \tag{2.25}$$

where a_2 and a_3 are the group velocity variation and 3^{rd} order dispersion. a_2 and a_3 can be found out by introducing a sharpness metric function $M(a_2, a_3)$, which is maximized when the image is sharpest.

2.2 Doppler Optical Coherence Tomography (DOCT)

2.2.1 Introduction

Doppler optical coherence tomography (DOCT) is a variation of OCT which combines the Doppler principle with OCT and provides *in-vivo* imaging of speed and direction of blood flow in vessels [13]. The concept of DOCT was first suggested by Nelson et al. in 1995 [14] in which the centroid method to calculate the mean Doppler spectrum shift was introduced. In the following next few years, advancements of DOCT in terms of algorithms were made, such as color Doppler imaging method introduced by Izatt [15] and Chen's work on phase-resolved DOCT method by using Hilbert transform [16]. Before the invention of FD-OCT, all the DOCT studies were done with TD-OCT. In 2003 Leitgeb, et al., demonstrated the first phase-resolved technique with SD-OCT [17].

Blood flow in organisms is complicated. The flow velocity profile depends on a many different factors: species, type of organs, body temperature, heart beat rate, vessel size…to mention just a few. For humans and other mammals, the blood flow is pulsatile and the speed varies from the centre to the edges in any blood vessel. In fluid dynamics, different flow patterns can be characterized by the Reynolds number Re:

$$\mathrm{Re} = \frac{\rho v L}{\mu} \tag{2.26}$$

where ρ is the fluid density, v and μ are the mean velocity and viscosity of the fluid, L is the characteristic linear dimension. In the case of low Re, the blood velocity can be described as parabolic distribution along the blood vessel radius, which is also known as laminar flow; for

high Re where the speed is high, it can lead to the chaotic turbulent flow. Unlike laser Doppler velocimetry in which mostly a monochromatic light source is used, in Doppler OCT a broadband light source is used while the backscattered light by a moving element in the sample will produce a spectrum of Doppler frequencies instead of just a single frequency. The information of Doppler frequency shift can be displayed either by color Doppler method or variance method [13]. In the color Doppler imaging method, the Doppler frequency shift of all the elements in a sample is displayed as a color image, where the positive and negative frequency shifts are displayed in different colors, say, blue for positive and red for negative, which provide quantitative information on the flow speed and flow direction. In a Doppler variance image, the variance or the standard deviation of the Doppler frequency shift is displayed and it can be used to quantify not only blood flow but also Brownian motion [13].

2.2.2 Phase Resolved Method

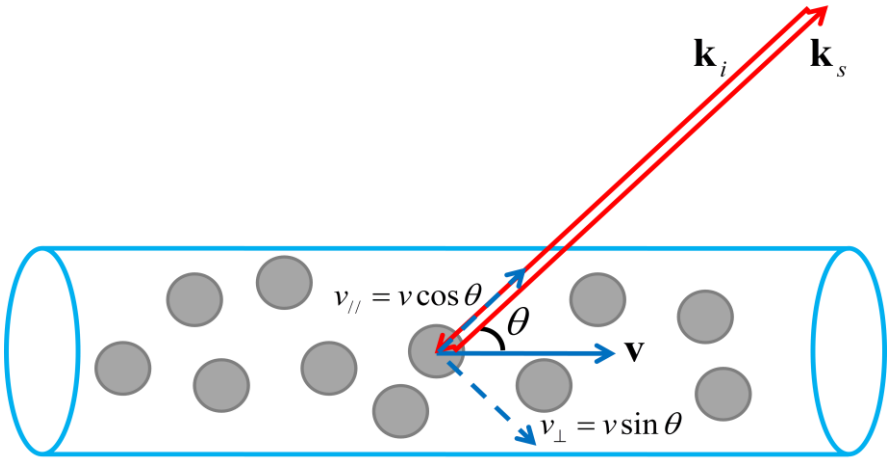

Fig. 2.5 Schematic of flow direction and imaging beam angle.

Fig. 2.5 shows a sketch of how the Doppler frequency f_D and blood flow velocity $\mathbf{v}$ are measured by an imaging beam. f_D is related to the wavevectors of the incident and backscattered beam, $\mathbf{k}_i$ and $\mathbf{k}_s$, by

$$f_D = \frac{1}{2\pi}(\mathbf{k}_s - \mathbf{k}_i)\cdot\mathbf{v} \tag{2.27}$$

In terms of angle θ between the imaging beam and the flow direction, Δf can also be written as

$$\frac{f_D}{f_0} = \frac{2v_{//}}{c} \quad \Rightarrow \quad f_D = \frac{2v\cos\theta}{\lambda_0} \tag{2.28}$$

where f_0 and λ_0 are the center frequency and wavelength in vacuum of the light source. In Doppler OCT, the Doppler frequency of every element in an OCT image is determined separately. This can be done by introducing the phase-resolved method [13] using Kasai velocity estimator [18]. Consider a situation in which we attempt to measure the blood flow in biological tissue with a SD-OCT system. The spectrum $S(k,x)$ collected by the CCD camera with *M* pixels can be processed as an OCT image by using Fast Fourier Transform (FFT):

$$\tilde{I}(z,x) = \mathrm{FFT}^{k\to z}\left\{S(k,x)\right\} \tag{2.29}$$

where *k* and *z* are the pixel numbers along which represents wavenumber and axial depth before and after FFT, while *x* is the pixel number representing different A-scans. Notice that after applying FFT on $S(k,x)$, $\tilde{I}(z,x)$ itself is a complex number with phase $\phi(z,x)$:

$$\tilde{I}(z,x) = I(z,x)\exp\left[i\phi(z,x)\right] \tag{2.30}$$

Suppose the total number of A-scans is large enough such that for adjacent x^{th} and x+1^{th}A-scans the imaging beam still hits on the same blood vessel. The mean Doppler frequency $\bar{f}_D$, which is also the average of power spectrum shift, is related to the rate of phase change $d\phi/dt$:

$$\bar{f}_D = \frac{\int f_D P(f_D) df_D}{\int P(f_D) df_D} = \frac{d\phi}{dt} \tag{2.31}$$

In discrete form, this becomes the phase difference $\Delta\phi_{z,x}$ between adjacent A-scans after taking FFT [13], while $\Delta\phi_{z,x}$ can easily be found by multiplying the x+1^{th} A-scan with the conjugate of x^{th} A-scan:

$$\bar{f}_D(z,x) = \frac{\Delta\phi_{z,x}}{2\pi T} = \frac{\phi_{z,x+1} - \phi_{z,x}}{2\pi T} = \frac{\arg(\tilde{I}^*_{z,x}\tilde{I}_{z,x+1})}{2\pi T} \tag{2.32}$$

where T is the period of A-scan, which is also called A-line rate. Substitute with Eq. (2.28), the axial and absolute velocities can be expressed in term of the phase change:

$$v_{//}(z,x) = \frac{\lambda_0 \Delta\phi_{z,x}}{4\pi nT} \tag{2.33}$$

$$v(z,x) = \frac{\lambda_0 \Delta\phi_{z,x}}{4\pi nT} \frac{1}{\cos\theta} \tag{2.34}$$

To demonstrate the reliability of DOCT phase-resolved method of analyzing retinal blood flow, a phantom test was carried out and the details are written in Appendix A.

2.3 Optical Micro-Angiography (OMAG)

2.3.1 Introduction

For instance, DOCT has been able to perform non-invasive quantitative imaging of subsurface blood flows at high spatial and temporal resolutions. However, DOCT has suffered under excessive phase noise, which may be attributed to dynamic multiple scattering speckle noise, biological tissue heterogeneity, motion artifacts and shot noise from CCD spectrometers. To resolve the issue, Optical Micro-Angiography (OMAG) as a variation of SD-OCT was invented. OMAG is used to visualize the blood perfusion distribution by removing other static biological tissue and other unwanted types of noise in OCT images. There are many different versions of the OMAG method, differentiated in terms of the OCT system design, the imaging protocols and the algorithms used to process the OCT images. All of those methods can be applied to achieve perfusion visualization of blood vessels in different types of biological tissue, such as human skin, human retina [19], [20], rat retina [9], [21] and brain cortex of mice [22]. OMAG was firstly demonstrated by Yasuno et al. in human retina in 2006 [23], where an OCT intensity binary mask was applied to filter out the static tissues during color Doppler image processing. Wang et al. in 2007 introduced a frequency modulation method to differentiate perfusion from static tissues by linearly scanning the reference mirror with a PZT translator [24], while later such method was further improved by actuating an off-center galvanometric mirror in the sample arm. Other OMAG techniques include digital frequency modulation [25], [26], single-pass with modified Hilbert transform [27], [28] and differential spectrum by taking two B-

scans in one y-step [9]. Combined with phase-resolved method, OMAG can be further extended as Doppler OMAG (D-OMAG) [29], which is capable to do quantitative analysis of blood perfusion such as measurements of Doppler frequency, velocity and flow rate.

2.3.2 Digital Frequency Ramping Method (DFRM)

In the early stages of OMAG development, a frequency modulation is applied physically to the OCT imaging system in order to separate perfusion from static tissues when doing Fourier Transform on the CCD spectrum. Such physical modulation can either be done by linearly oscillating the reference mirror with a PZT translator [24] or by actuating an off-center galvano mirror in the sample arm [19]. However, both methods require either extra cost for purchasing equipment or additional optical alignment of the sample arm. To resolve those drawbacks, Wang [25] and Yuan [26] have developed a digital frequency modulation technique, also known as Digital Frequency Ramping Method (DFRM). This method works very well in perfusion visualization, plus it is algorithmically easy to programme, computationally fast and does not require extra modification of optics or imaging protocols. Therefore DFRM is adopted as the OMAG technique used in this thesis.

The principle of operation of the DFRM method mentioned below is based on references [25] and [26]. The purpose of DFRM is to mathematically map the blood vessels and static tissues to the positive and negative (conjugate) time delay sides of the B-scan image. Consider we are imaging a biological tissue with perfusion with repeating A-scans scanning in a transverse direction. By taking only the cross-correlation term into account, the interferometric signal $S'_x(k,\Delta z)$ of the x^{th} A-scan with respect to one moving scatterer (e.g. a particle in the blood vessel) from depth Δz in the sample can be rewritten as

$$S'_x(k,\Delta z) = 2S(k)\sqrt{a_r a_x(\Delta z)}\cos\left[2k\Delta z + \phi + 2\pi(f_s + f_d)\cdot xT\right] \tag{2.35}$$

where a_r and $a_x(\Delta z)$ are the attenuation coefficients of the backscattered light from the reference mirror and the scatterer from depth Δz in the sample respectively. f_s and f_d are the Doppler frequencies corresponding to the bulk motion of the sample and blood flow respectively. $S(k)$ is the spectrum of the imaging light source, k, T and ϕ are the wavenumber, A-line rate and random phase due to scattering biological tissue. For convenience, the amplitude term is simplified as

$2S(k)\sqrt{a_r a_x(\Delta z)} = A_x(k,\Delta z)$.The first step of DFRM is to introduce a phase shift to $S_x'(k,\Delta z)$, which can be numerically done by using Hilbert transform in *k*-space:

$$\tilde{S}_x(k,\Delta z) = H_k[S_x'(k,\Delta z)] = A_x(k,\Delta z)\exp\left\{i\left[2k\Delta z + \phi + 2\pi(f_s + f_d)\cdot xT\right]\right\} \quad (2.36)$$

By adding a digital modulation Doppler frequency f_m to Eq. (2.36), it becomes

$$\tilde{P}_x(k,\Delta z) = A_x(k,\Delta z)\exp\left\{i\left[2k\Delta z + \phi + 2\pi(f_s + f_d - f_m)\cdot xT\right]\right\} \quad (2.37)$$

Consider only the real part,

$$P_x(k,\Delta z) = A_x(k,\Delta z)\cos\left[2k\Delta z + \phi + 2\pi(f_s + f_d - f_m)\cdot xT\right] \quad (2.38)$$

Here we define two terms. If f_m is suitably chosen such that $f_s < f_m < f_s + f_d$, the net frequency in a static tissue and blood vessel are $\Delta f_{s,m} = f_s - f_m < 0$ and $\Delta f_{d,m} = f_s + f_d - f_m > 0$ respectively. Then by taking Hilbert transform of $P_x(k,\Delta z)$ in the transverse direction,

$$\tilde{P}_x'(k,\Delta z) = A_x(k,\Delta z)\exp\left\{i\left[2k\Delta z + \phi + 2\pi\Delta f_{s,m}\cdot xT\right]\right\} \quad (2.39)$$

$$\tilde{P}_x'(k,\Delta z) = A_x(k,\Delta z)\exp\left\{i\left[2k\Delta z + \phi + 2\pi\Delta f_{d,m}\cdot xT\right]\right\} \quad (2.40)$$

where Eqs. (2.39) and (2.40) have negative and positive phase modulations respectively. Finally by taking inverse Fourier Transform along the axial direction,

$$I_x(\Delta z) = \mathrm{IFT}\left\{\tilde{P}_x'(k,\Delta z)\right\} \quad (2.41)$$

which will allow for reconstruction of the OMAG image $I_x(\Delta z)$ in which the blood perfusion locates in the positive side ($z > 0$), while the static tissue locates in the negative side ($z < 0$). Since the modulation frequency f_m is digital, it can be adjusted by trial and error until a best value is obtained to differentiate the perfusion from static tissue. Therefore in principle DFRM is suitable for OMAG imaging of various types of biological samples with different morphological structures and bulk movements.

Chapter 3

Outer Retina Degeneration

3.1 Human Outer Retina Degenerative Disease and Animal Model

Currently, there are number of retinal degeneration diseases which could potentially lead to blindness: age macular degeneration (AMD), retinitis pigmentosa (RP), diabetic retinopathy and glaucoma. Two of these diseases, AMD and RP, tend to originate and develop primarily in the outer retina, affecting the structural integrity of the photoreceptors and retinal pigmented epithelium (RPE) cells, as well as causing changes in the choroidal capillaries (CC). AMD disrupts the vision of elderly people progressively by affecting the oval-shaped highly pigmented yellow spot at the centre of the retina which is also known as macula. Within the macula is the fovea with high concentration of cone photoreceptors that plays a main role in high resolution vision. There are two types of AMD: "dry" and "wet", or more formally, central geographic atrophy (CGA) and choroidal neovascular AMD (CNV-AMD). CGA results from exhaustion of retinal pigment epithelium (RPE) cells in the macula due to loss of rods and cones photoreceptors [4], while CNV has abnormal blood vessel growth of choroidal capillaries which also leads to vision loss [6]. RP is a retinal dystrophy due to progressive loss of photoreceptors and abnormal functionality of RPE which also leads to blindness [30].

In order to study the progress of eye diseases in detail, as well as to develop novel treatments and medicines for testing, animal models are widely used by researchers. Rats and mice are the most common animal subjects in the laboratories thanks to their mammal nature same as humans, small in size, easy to handle, inexpensive costs and fast metabolism rate that experimentally induced diseases can take effect within much shorter period of time. There are many ways to intentionally induce retinal degeneration in rats. Depending upon the methods, retinal disease models are used to study the malfunction of different parts in the retina, such as optic neuropathy in the optical nerve head, perfusion in the CC, RPE function or structural change of photoreceptors. Those disease models can be either light induced such as using high intensity laser pulses to simulate CNV-AMD [7]; physically induced such as raised intra-ocular pressure to simulate glaucoma [9]; or chemically induced such as sodium iodate to simulate photoreceptor disruption [10], [11].

3.2 Sodium Iodate ($NaIO_3$) Model of Outer Retina Degeneration

Sodium iodate ($NaIO_3$) is the sodium salt of iodic acid which appears as whitish powders and used as an oxidizing agent. In 1941, Sorsby first discovered that $NaIO_3$ can cause pigmentary degeneration of the retina [31]. RPE has a number of functions such as shielding the retina from excessive incident light, supply glucose, maintain vitamin A cycle, phagocytises older outer segments and secure the adhesion of the retina with the choroid. $NaIO_3$ is particularly toxic to the RPE cells by disrupting its functionality, which leads to degeneration of the photoreceptor. The details about the effect of $NaIO_3$ toxicity on morphology, visual functionality and blood perfusion are listed in the text below.

As one of the observable early effects, the $NaIO_3$ toxicity first reduces the adhesive force between the RPE and the neural retina. Electron microscopy images captured from pigmented rabbits' retinas showed a ~50% decrease of adhesive force just 10 minutes after the $NaIO_3$ injection, especially at the level of the Bruch's membrane, while such detachment became more significant at ~100 minutes post injection [32]. Such study also showed the $NaIO_3$ drug tends to firstly affect the adhesion of the basal aspect of the RPE, and then the apical aspect afterwards. As time goes longer, the $NaIO_3$ toxicity causes RPE degeneration and disorganization of the photoreceptor layer, shown by electron and light microscopy images captured from C57BL mice [33]. The number of RPE cells decreased at 12 hours post injection, while further damage in RPE cells and disorganization of the photoreceptor layer were observed at 24 hours post-injection. At day 3 post injection, the RPE layer could no longer sustain its continuity in which the RPE cells were replaced by a thin layer of melanin along Bruch's membrane. The thickness of the photoreceptor layer, including both inner and outer segments, was increased by ~50% at 24 hours post-injection but recover at day 3. Afterwards a gradual decrease lasted until 4 weeks later in which the thickness was reduced by ~80% [34]. Similar study was also done on imprinting control region (ICR) mice, where irregular shape of RPE and disorganization of outer segments were also observed along with extended destruction of the neurosensory retina at 24 hours post-injection [35]. Besides photoreceptor, ONL's cell number and thickness can also be reduced up to ~50% under a higher dose of $NaIO_3$ injection, shown by C57BL/6 mice at day 3 [34] and Sprague Dawley rats at day 7 [36], while on the other hand, the thicknesses of INL and GCL are not affected by the $NaIO_3$ toxicity.

As the RPE degeneration and photoreceptor disorganization carry on in a long term basis, the $NaIO_3$ toxicity would also blurred the boundary between the inner and outer segment in which they eventually become indistinguishable. This is shown by histological cross-sections on albino and pigmented rats and mice at one week post-injection [33]. Compared with the central region of the outer retina, the peripheral retina was less affected. The reason behind such difference is still unknown, but one possible reason was different metabolism of the drug by the central and peripheral cells in the retina as well as different degree of RPE cells regeneration potential in these regions [37]. Such study also showed $NaIO_3$ toxicity causes more severe damage on albino retinas than pigmented retinas, which might be attributed to the interaction between light and $NaIO_3$ [38]. It was possible that melanin in pigmented retinas absorbed the incident light and reduced the damage due to light-drug interaction, while albino retinas did not have such protection. Hariri et al. observed morphological retinal change of $NaIO_3$ treated Long Evans rats by using an UHR-OCT system in the 3 months study [10] and the short term study [11]. Part of the work in this thesis was published in [11], which imaged the retinas of 5 Long Evans rats at baseline and 1, 3, 6, 12 hours post injection. This measurement combined with the work of Hariri showed the photoreceptor and RPE degeneration can be observed by OCT technique.

Besides photoreceptor and RPE layer, $NaIO_3$ toxicity also has a disruptive effect on the perfusion of choroidal capillaries. Indocyanine Green (ICG), a fluorescent dye used in ophthalmic angiography, was used to visualize such effect on pigmented rabbits [39]. ICG angiography was performed on pigmented rabbits at 3 hours post injection and leakage in the CC was indicated by hyper-fluorescence spots in electron microscopy images. Such ICG leakage got expanded to the entire region at 24 hours post injection, reduced one week later and returned to normal at two weeks post injection with the RPE layer being severely damaged. At 4 weeks post injection, the CC was reduced in number along with the RPE cells, while at 11 weeks post-injection, CC in affected regions were surrounded by abnormally dense collagenous connective tissue. In the regions with loss of RPE cells, there was a reduction or even absence of CC, while for regions with healthy RPE cells the CC also looked normal. Therefore this study demonstrated a possible correlation between the reduction of CC and the damage of RPE cells, in which the CC depend on RPE cells for survival. ICG gives very high contrast images, however it is an invasive measurement technique, since it requires the injection of a dye IV away from the eye,

which means it takes time for the dye to reach the retina and provide full contrast. In addition, the image contrast deteriorates over time fairly fast, since the dye amount in the retina is progressively washed out with the blood circulation. Therefore, there is a need for a novel imaging modality that can image retinal vasculature and measure retinal blood flow non-invasively, such as DOCT.

After the degeneration under effect of $NaIO_3$ toxicity, the visual function could be partially recovered [33], but due to the initial malfunction of RPE, in overall it still causes a permanent damage to the outer retina and loss of visual acuity of the animal. Electroretinography (ERG) is one of the techniques commonly used by ophthalmologists to diagnose various retinal diseases. It quantifies the visual functionality by measuring the electrical responses of different types of cells in the retina under light stimulation with different colors and intensities, including the rod and cone cells in the photoreceptors; bipolar, amacrine and ganglion cells. ERG can be combined with a variation of OCT known as functional OCT (FOCT), which measures the intrinsic optical signal (IOS) of retinal layers under light stimulation. The electrical signal of ERG was shown to have strong correlation with the IOS measured by FOCT in chicken retina [40]. ERG tests were carried on injected rabbits, rats and mice to show their decline and loss of vision under $NaIO_3$ toxicity [35], [36], [41], [42]. There are two kinds of electric signals in ERG, named a-wave and b-wave respectively. a-wave is a negative potential produced by the photoreceptors, while b-wave is a positive potential produced by the mixture of the responses from photoreceptors, biopolar, amacrine and Muller cells. From the study of $NaIO_3$ injected Sprague-Dawley rats in reference [36], the magnitude of b-wave decreased over the entire range of stimulus intensities at day 7 post-injection and such reduction was more significant with higher dose. The a-wave magnitude increased with higher dose at day 7, but eventually decreased and almost vanished at day 28. For the study in reference [41] using BALB/c mice as subjects, the a and b-waves response were almost zero at day 7, but recovered slowly starting at day 14 until the end of the study at day 42. This showed there was a slow recovery of RPE cells to restore the visual function partially. Nevertheless, the ERG response at the end was still smaller than that before injection.

To conclude, $NaIO_3$ severely damages the retina by degeneration of RPE cells; disorganization, thickness reduction of photoreceptor layers; detachment between the RPE layer

and the neuron retina; leakage and atrophy of choroidal capillaries. The $NaIO_3$ model cannot completely simulate the actual human retinal diseases such as AMD or RP. For example, in $NaIO_3$ model, Bruch's membrane remains unchanged under toxicity and the RPE is affected before photoreceptor cells. In realistic diseases, AMD causes death of RPE cells by depositing lipofuscin on Bruch's membrane, while RP has photoreceptor cells death first before RPE cells. However, $NaIO_3$ toxicity still serves as a useful model due to its inexpensive cost and retinal degeneration is controllable by adjusting the dose amount, which can still mimic different degrees of progression of retinal diseases if the model is designed appropriately.

3.3 Potential Change in Inner Retinal Blood Flow?

OCT has been used for a long time as an *in vivo*, non-invasive method to image rodent retinas under different disease models. However, it has not been used to test the $NaIO_3$ treated retinas until the work of Hariri et al. in recent years [10], [11]. This thesis is a continuation of the PhD thesis work of S. Hariri, which utilised for the first time UHR-OCT system to image and evaluate acute and long-term structural changes in $NaIO_3$ treated of Long Evans rats' retina. In addition, up to date there is no report about $NaIO_3$ toxicity on damaging in the inner retinal structure. The morphology of all inner retinal layers seems to be normal according to several papers [33], [36], [37], [41]. This thesis aims to use the combination OMAG and Doppler OCT, two variations of OCT imaging method, to quantitatively determine if the blood flow in the inter retina, the choroid and the optical nerve head in rats can be affected by $NaIO_3$ toxicity.

Chapter 4

Methods

4.1 Spectral Domain OCT System

A compact, fiber-optic SD-OCT system, designed and built in Dr. Bizheva's research lab, was used for the $NaIO_3$ induced rat retina degeneration study. The schematic of the system is shown in Fig. 4.1.

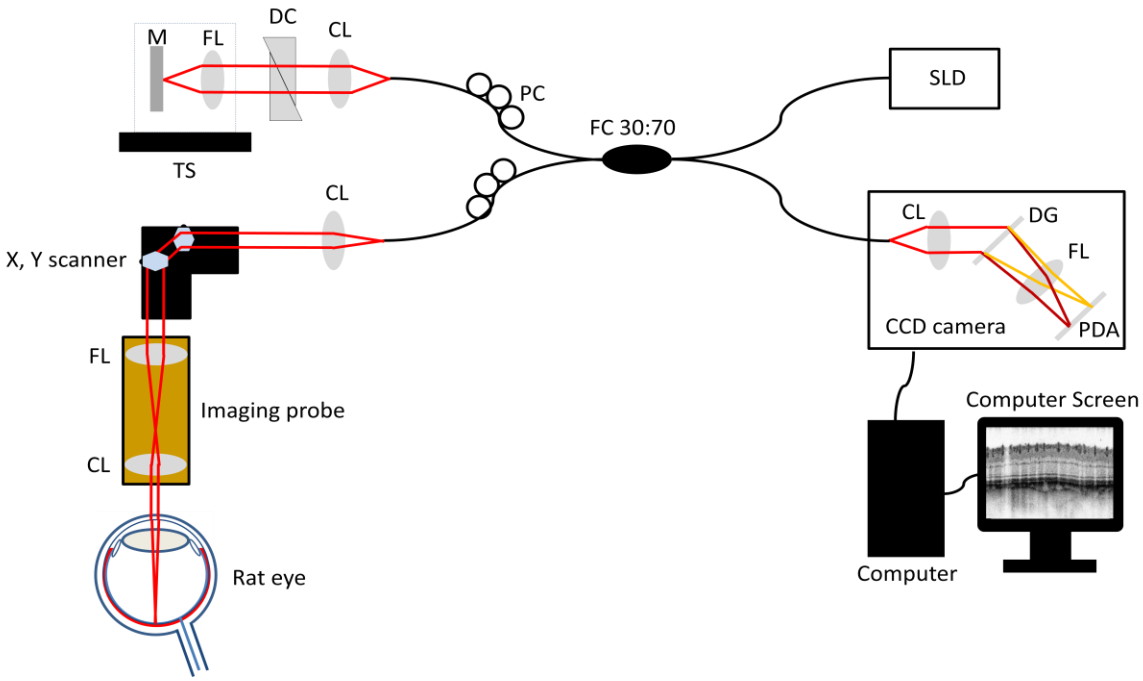

Fig. 4.1 Schematic of the ultrahigh-resolution SD-OCT system. Abbreviations of system components are: SLD - superluminescent diode, FC - fiber coupler, PC - polarization controllers, CL - collimating lens, DC - dispersion compensation unit, TS -translation stage, M - mirror, FL - focusing lens, DG - diffraction grating, PDA - photodetector array.

Refer to Fig. 4.1, a superluminescent diode (SLD, Superlum Inc.) with central wavelength $\lambda_0 = 1020\,\text{nm}$ and FHHM $\Delta\lambda = 110\,\text{nm}$ is used as the light source. It has an output power of $P_0 = 10\,\text{mW}$ before entering the fiber coupler. Both reference and sample arms have polarization controller (PC) units with three loops in each unit. The polarization has to be adjusted not only to match the spectral shape for both arms but also to optimize the PSF and quality of the OCT

image. Besides the PC, the reference arm also includes a pair of lenses to focus the beam on the reference mirror and a dispersion compensation double prism unit to match the dispersion in both arms, while the sample arm also includes a collimating lens, a pair of X-Y galvanometric scanners (Cambridge Technology Inc.) and an imaging probe with two lenses (Edmund Optics) to reduce the spot size of the imaging beam. The combined signal from the two arms is fed into a spectrometer (P&P Optica Inc.) and A CCD camera (SUI Goodrich) with a 1024 pixel linear array is used as the photo-detector. The spectrometer covers a spectral range of $940-1120\,\text{nm}$, with spectral resolution of $\delta\lambda = 0.15\,\text{nm}$ and diffraction efficiency of grating over 80%. The OCT system was measured to have a SNR of $\sim 99\,\text{dB}$ with imaging beam of $1.6\,\text{mW}$ power in the sample arm [11]. A computer (Intel Xeon, 3.6 GHz, 2GBRAM) is connected to the CCD camera via a frame grabber (National Instruments, PCIe-1429). A LabVIEW routine was used to carry out the OCT data acquisition, while a MATLAB code was written to process the morphological and Doppler OCT images.

4.2 Sample Arm

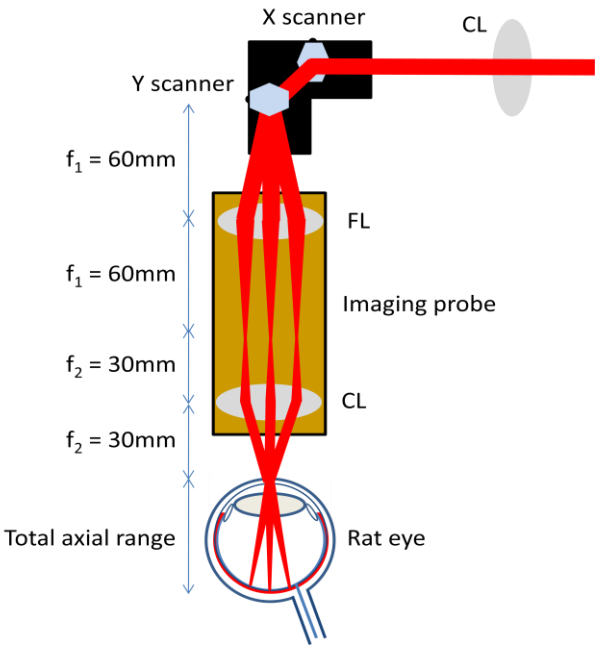

Fig. 4.2 Schematic of the sample arm used for rat retina OCT imaging. Abbreviations of system components are: CL - collimating lens, FL - focusing lens. The first CL produces a collimated beam on the X-Y scanners, while the FL and second CL reduce the spot size of the beam by ~50% before entering the rat eye. The X-Y scanners are controlled by a LabVIEW routine to direct the beam to scan over different positions of the retina.

Refer to Fig. 4.2, the sample arm consists of 3 achromatic lenses, one acts as a collimating lens to produce a parallel beam on the X-Y scanners, while another two act as collimating and focusing lens in the sample probe, with focal lengths $f_1 = 60\,\text{mm}$ and $f_2 = 30\,\text{mm}$ respectively, to reduce the size of the beam spot by ~50% before entering the pupil of the rat eye. After passing through the probe, the spot size is ~1.2mm in diameter, which corresponds to a transverse resolution of 3.2 μm. By assuming the refractive index in the rat eye $n = 1.35$, the axial resolution in the rat retina is estimated to be 3μm.The X-Y mirrors, with maximum sweeping angle of 20°, are controlled by a LabVIEW routine to direct the beam to scan over different positions of the retina in order to produce a 3D morphological and Doppler OCT image.

4.3 Animal Handling and Preparation

The animal experiments were conducted in accordance with the ethical regulations of the University of Waterloo Animal Care committee. Seven Long Evans rats were used in this study. Retinal degeneration was induced by injection of 40mg/kg of $NaIO_3$ solution. During imaging, the rats were put to sleep using an anaesthesia system which provided 2.5-3% of isoflurane mixed with 0.8L/min of oxygen gas fed to the nose of each rat. 1 to 2 drops of tropicamide (Mydriacyl, 1%) were used to dilate the pupil of each rat's eye. Artificial hydration drops were put on the rat's eye not only to maintain the moisture but also to keep the cornea optically clear enough for imaging. Warming pads were used to maintain the rat body temperature within $38-40^\circ\text{C}$, while thermometer and oxymeter were used to frequently check the body temperature, oxygen level and heart beat rate of the rat under anaesthesia. The seven rats were divided into two groups, with 5 rats in group A which were used to investigate the morphological change during retinal degeneration within 12 hours, while 2 rats in group B were used to investigate both morphology and blood flow under retinal degeneration within one week. Rats in group A were anaesthetized before $NaIO_3$ injection and 1, 3, 6, 12 hours post injection, while rats in group B were anaesthetized before injection and at 1, 3, 6 12, 24, 72, 168 hours post $NaIO_3$ injection.

4.4 Imaging Protocols, Acquisition and Processing

All the imaging protocols were set and carried out using a LabVIEW code. The X-Y scanners and CCD camera were adjusted to have an A-line rate of 47 kHz. For group A, 1000 A-scans times 256 B-scans were used in the linear scan imaging protocol to produce high resolution, high contrast morphological 3D OCT images [11]. Two different X-Y mirrors scanning ranges, 15° and 8°, were used and their field of views (FOVs) in the rat retina were estimated to be ~1.9mm and ~1.0mm respectively. For group B, we used a circular scan imaging protocol similar to the one Y. Wang, et. al., conducted in 2008 [43] to acquire the blood flow of all the ONH vessels within a short time interval. Circular scan was applied around the ONH with 3000 A-scans. The X-Y mirrors had 7° of scanning range which corresponded to a FOV ~2.8mm. In order to reduce the error due to motion artifact and speckle noise, 200 repetitive B-scans were applied around the same location for averaging [9]. Using this imaging protocol, both morphological and phase-resolved images were acquired simultaneously. Besides circular scanning, in order to determine the Doppler angle in each vessel, linear scanning was also done with 1000 A-scans times 1000 B-scans and 14° of X-Y mirrors scanning range which corresponds to FOV ~1.77mm. The time required to switch between circular and linear scanning mode in LabVIEW was about 10 s.

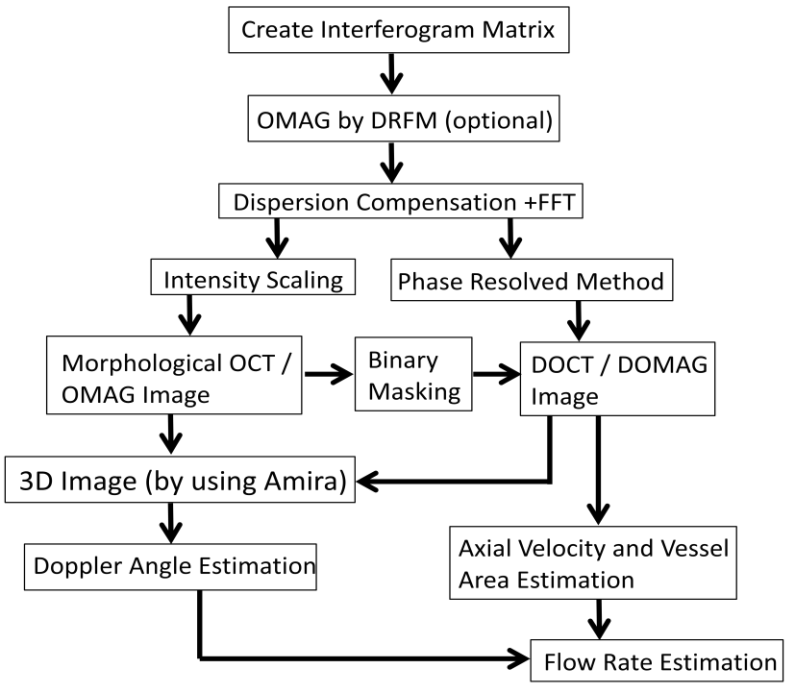

Fig. 4.3 A flow chart showing the OCT data processing. A MATLAB Graphical User Interface (GUI) was written to produce 2D morphological OCT, DOCT, OMAG and DOMAG images. The GUI creates a 2D morphological image by converting the raw data (acquired from LabVIEW) into an interferogram matrix, followed by dispersion compensation, FFT and intensity scaling. OMAG image can be created instead if DRFM algorithm is applied before dispersion compensation. If phase-resolved algorithm is applied right after FFT, a DOCT and a DOMAG image are created by multiplying the resultant matrix with a binary mask converted from morphological OCT and OMAG image respectively. 2D stack of morphological or OMAG linear scan images form a 3D image by using the Amira software and Doppler angles of all ONH vessels are estimated. Together with the axial velocity and vessel area estimated from the circular scan DOMAG image, the flow rates of all ONH vessels are estimated.

A MATLAB code was written based on the algorithms published in references [12], [13], [23] and [26] to generate different type of 2D OCT images(morphological OCT, DOCT, OMAG and DOMAG). Fig. 4.3 is a flow chart showing the OCT data processing. An interferogram matrix $S(k, j)$ is produced first, with k is the axial pixel number which represents the wave number, j corresponds to the j^{th} A-scan. $S(k, j)$ can be transformed into $S'(k, j)$ by applying a DFRM OMAG method here. Afterwards dispersion compensation and FFT along the axial direction are applied on $S(k, j)$ or $S'(k, j)$. By adjusting intensity scales, the morphological OCT or OMAG image, $I(i, j)$ or $I'(i, j)$, are obtained, where i is the pixel number that represents the axial distance. If phase resolved method is applied just right after FFT, combined

with a binary mask $J(i, j)$ produced from $I(i, j)$ or $I'(i, j)$, the DOCT or DOMAG image, $D(i, j)$ or $D'(i, j)$, are obtained.

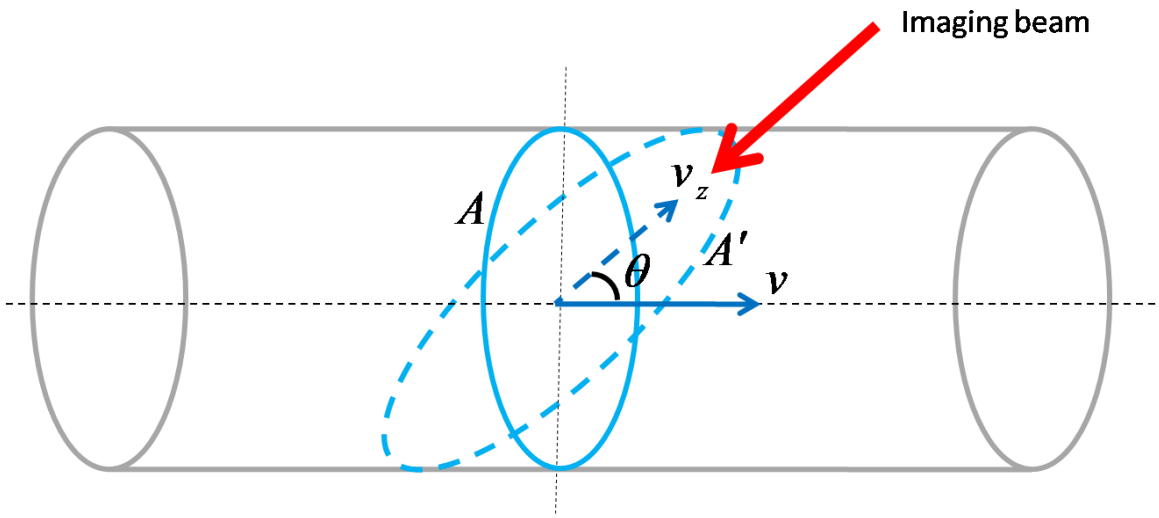

Fig. 4.4 A schematic showing the flow rate estimation of a blood vessel.

The axial velocity and vessel area of each ONH vessel in rat's retina are estimated using the circular scan DOMAG images. 3D images are produced from linear scan morphological OCT or OMAG images using Amira software, where the Doppler angle for each ONH vessel is estimated. Fig. 4.4 illustrates how to estimate the flow rate in a blood vessel. The flow rate F is defined as

$$F = \sum_{i,j} v(i, j)\Delta A(i, j) \tag{4.1}$$

At the position (i, j), $v(i, j)$ is the absolute velocity with its direction parallel to the vessel, $\Delta A(i, j)$ is the vessel area with its normal also parallel to the vessel. From a DOMAG image, what can be directed measured are the axial velocity $v_z(i, j)$ parallel to the imaging beam and the cross-sectional area $\Delta A'(i, j)$ with its normal perpendicular to the imaging beam. If the vessel has a Doppler angle θ with the imaging beam, the parameters above can be related as $v(i, j) = v_z(i, j) / \cos\theta$ and $\Delta A(i, j) = \Delta A'(i, j)\sin\theta$. Therefore the flow rate can be expressed as

$$F = \sum_{i,j} v_z(i, j)\Delta A'(i, j)\tan\theta \tag{4.2}$$

Chapter 5

Effect of Sodium Iodate Toxicity on Retinal Morphology and Optical Nerve Head Flow Rate of Rat

5.1 Photoreceptor Degeneration Observed in Morphological OCT Images

Fig. 5.1(a) is a representative 2D morphological OCT image acquired using linear scan mode at baseline for one of the rats. Before $NaIO_3$ injection, the retinal layers can be clearly identified, as indicated by the abbreviations at the left.

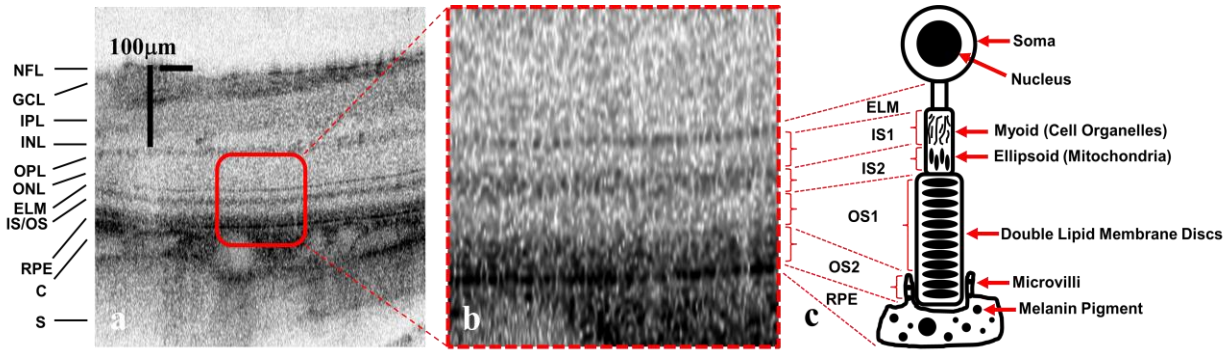

Fig. 5.1 (a) A representative 2D morphological image acquired from a healthy rat retina with all retinal layers clearly visualized and labeled. Abbreviations of retinal layers are: NFL - nerve fiber layer, GCL - ganglion cell layer, IPL - inner plexiform layer, INL - inner nuclear layer, OPL - outer plexiform layer, ONL - outer nuclear layer, ELM - external limiting membrane, IS - inner segment, OS - outer segment, RPE - retina pigment epithelium, C – choroid, S – sclera. (b) Magnified view of the PR and RPE layers, where the inner segment can be furthered divided as IS1 and IS2; the outer segment can be furthered divided as OS1 and OS2. (c) Schematic representation of anatomical features of the rod PR cell.

Fig. 5.1(b) is a magnified view of the outer retina at the area framed with a red dashed rectangle, while Fig 5.1(c) shows a sketch of a RPE and photoreceptor cell similar to those found in retinal anatomy books. As labeled in Fig. 5.1(b), the inner segment can be furthered divided as IS1 and IS2, while the outer segment can be furthered divided as OS1 and OS2. A pixel with a darker color in the tomogram indicates it has a higher reflectance. The thin ELM and RPE layers have high reflectance. IS1 and OS1 have relatively low reflectance while IS2 and OS2 have relatively high reflectance, which assemble as alternative low and high reflective bands. This can be correlated by a recent publication by Spaide and Curcio [44]. As shown in Fig. 5.1(c), the highly

relative ELM is composed of synapses of the Muller cells; IS1 is the myoid filled with transparent cytoplasm and cellular organelles such as microfilaments, Golgi apparatus and ribosomes that are less than 1μm in size, in which all those matters have relatively lower reflective indices; IS2 is the ellipsoid composed of densely packed mitochondria with much higher reflective index of ~1.4 compared with cellular organelles; OS1 is composed of upper part of double lipid membrane discs with relatively lower reflective index again; OS2 is the lower part of membrane discs adhered with the RPE cells, which is filled with microvilli cells containing melanin pigments of high optical refractive index of ~1.67; the RPE layer is composed of mainly melanin pigments and hence it has the highest reflectance compared with all the PR layers above. Morphological OCT images were acquired from all rats at baseline and 1, 3, 6, 12 hours post injection. The scanning was applied to approximately the same retinal area at every time point for each rat, where the baseline tomogram was used as a reference image to study any structural changes in the retina, especially PR and RPE layers, induced by $NaIO_3$ toxicity at different time points.

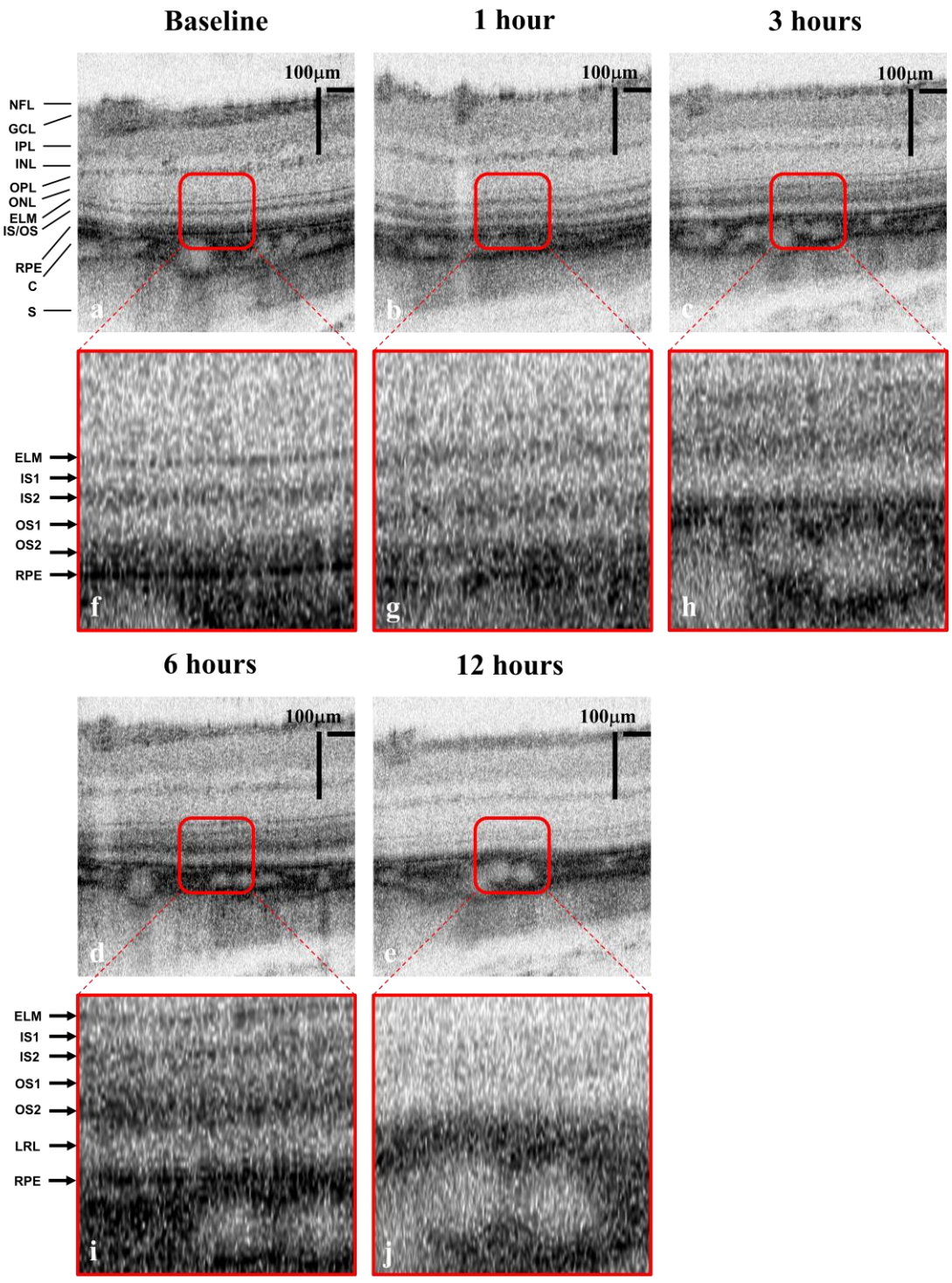

Fig. 5.2 (a) Representative 2D morphological OCT images acquired from approximately the same region of the central retina of rat E, showing progressive changes in the outer retina due to the toxic effect of the injected drug. Images (a) to (e) are acquired at baseline and 1, 3 6, 12 hours post $NaIO_3$ injection respectively. Images (f) to (j) are the 3× magnified view of these 5 time points.

In the morphological OCT study, 5 rats named A, B, C, D and E were used. Fig. 5.2(a), (b) (c), (d) and (e) show representative 2D morphological OCT images acquired using linear scan mode at all post $NaIO_3$ injection time points for rat E. The areas within the red frames are magnified 3× and shown in Fig 5.2 (f), (g), (h), (i) and (j). The baseline image has the PR layers same as Fig. 5.1. At 1 hour post injection [Fig. 5.2(b) and (g)], the refractive index of OS1 was increased compared with the baseline image, as shown by the darker band. This suggests there was most likely a rearrangement of the PR tissues in OS1 which leaded to an increase of light scattering and made it looked darker. More importantly, a very low reflective layer (LRL) started appear between the OS2 and the RPE layer. While the RPE layer looked structurally normal, the OS had been detached from the RPE. At 3 hours post injection [Fig. 5.2(c) and (h)], the OS1 and OS2 layers became homogeneous and could no longer be distinguished as two layers. The high reflectance, as indicated by the dark band, was possibly the rearrangement of OS tissues, membrane disks disruption, or both. At 12 hours post injection [Fig. 5.2(d) and (i)], apparently the IS and OS layer restored to alternative low and high reflective bands, similar to that of the retina before injection. However, the overall reflectance of the PR was reduced compared with the baseline image, as indicated by the faint color of the IS and OS. At the same time, the LRL also disappeared. Since every rat had a different body condition and metabolism, each individual responded differently under the $NaIO_3$ toxicity. Hence the time of appearance and disappearance as well as thickness of the LRL varied significantly for all rats used in this study.

In addition to the OCT images of rat E in Fig. 5.2, Figs.5.3-5.6 present OCT images acquired from rat A to D at different time points of the study. Since rat A to E were euthanized with their eyes enucleated for histology at baseline and 1, 3, 6 and 12 hours post injection respectively, images of each rat were only acquired up to the time point it was euthanized.

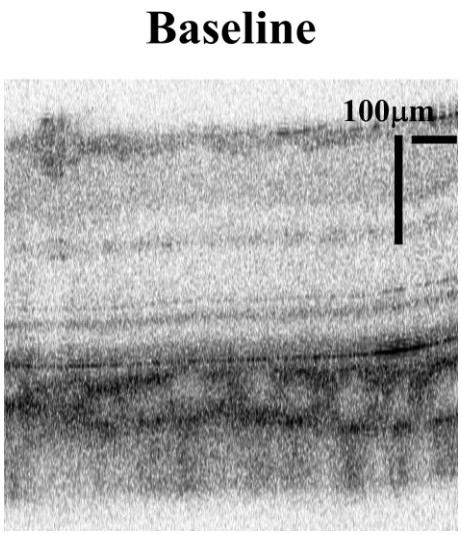

Fig. 5.3 A representative 2D morphological OCT image acquired from the central retina of rat A at baseline.

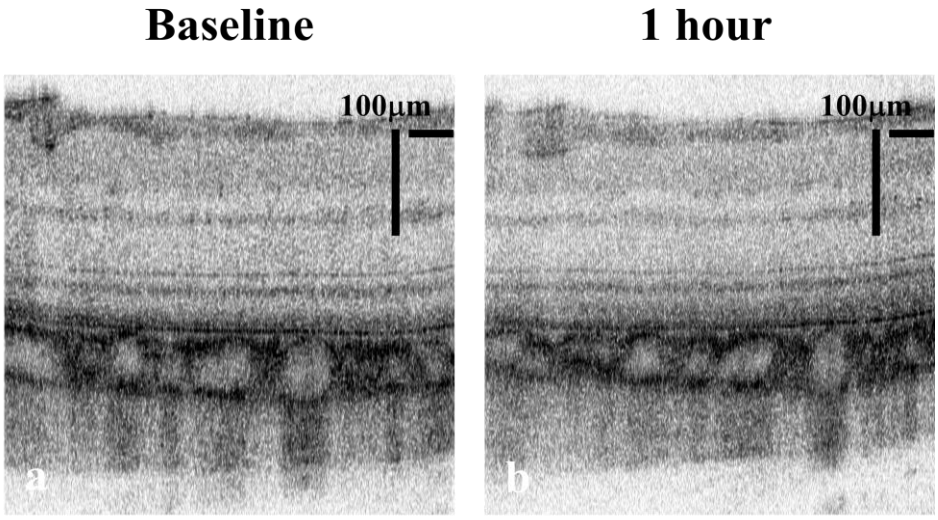

Fig. 5.4 Representative 2D morphological OCT images acquired from approximately the same region of the central retina of rat B. Images (a) and (b) are acquired at baseline and 1 hour post $NaIO_3$ injection respectively.

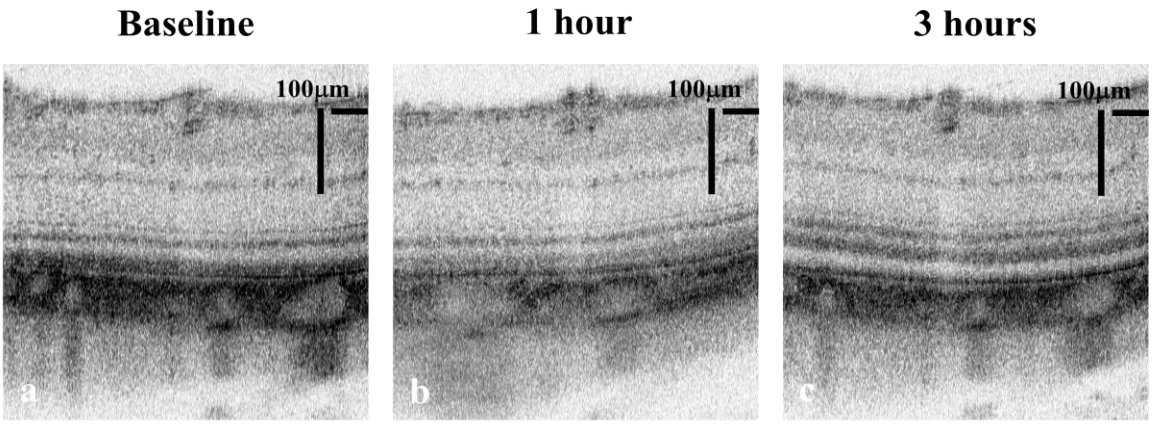

Fig. 5.5 Representative 2D morphological OCT images acquired from approximately the same region of the central retina of rat C. Images (a) to (c) are acquired at baseline and 1, 3 hours post $NaIO_3$ injection respectively.

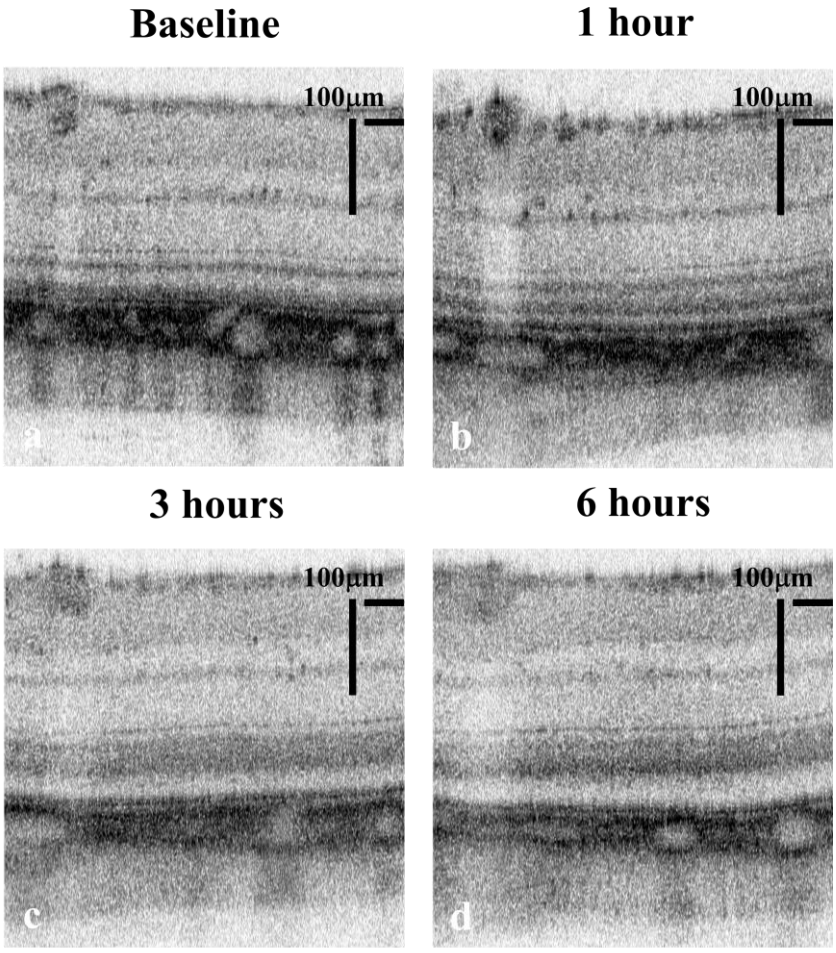

Fig. 5.6 Representative 2D morphological OCT images acquired from approximately the same region of the central retina of rat C. Images (a) to (d) are acquired at baseline and 1, 3, 6 hours post $NaIO_3$ injection respectively.

5.2 Comparison with Observation in Histological Images

Fig. 5.7 shows representative IgG and stained histological images acquired at different time points. The baseline H&E histological cross-section [Fig. 5.7 (a)] shows the typical normal appearance of the healthy rat retina with well identified retinal layers. In addition, Fig. 5.7(f) shows the labeling IgG protein remained as expected inside the retinal blood vessels (indicated by the black arrow), which suggested an intact blood-retina barrier. Swelling of the PR OS was observed in the histological cross-section at 1 hour post injection [Fig. 5.7(b)]. At 3 hour post injection [Fig. 5.7(c)], the toxic damage on the PR layer was even more significant, in which PR cells became large, fragile and pale due to hydropic change and weakened uptake of the H&E dyes. 6 hour post injection [Fig. 5.7(d)] had the most tremendous morphological change in which the fluid accumulation, which was confirmed to be the LRL in the OCT images mentioned above, caused complete separation of the OS2 from the underlying RPE. At the same time point, Fig. 5.7(f) also shows the immunohistochemistry image with substantial staining of IgG detected outside the lumen of inner retinal blood vessels, which confirms protein leakage as an outcome of the disruption of the blood-retinal barrier. The H&E histological cross-section corresponding to 12 hour post injection [Fig. 5.7(e)] looks similar to the one acquired at baseline [Fig. 5.7(a)] except for the swollen and broken RPE cells. Histological images of the $NaIO_3$ induced degeneration to the rat outer retina show very high consistency with morphological OCT images in terms of structural changes such as the retinal detachment, the presence of the new LRL and the altered retinal layers thickness and reflectance.

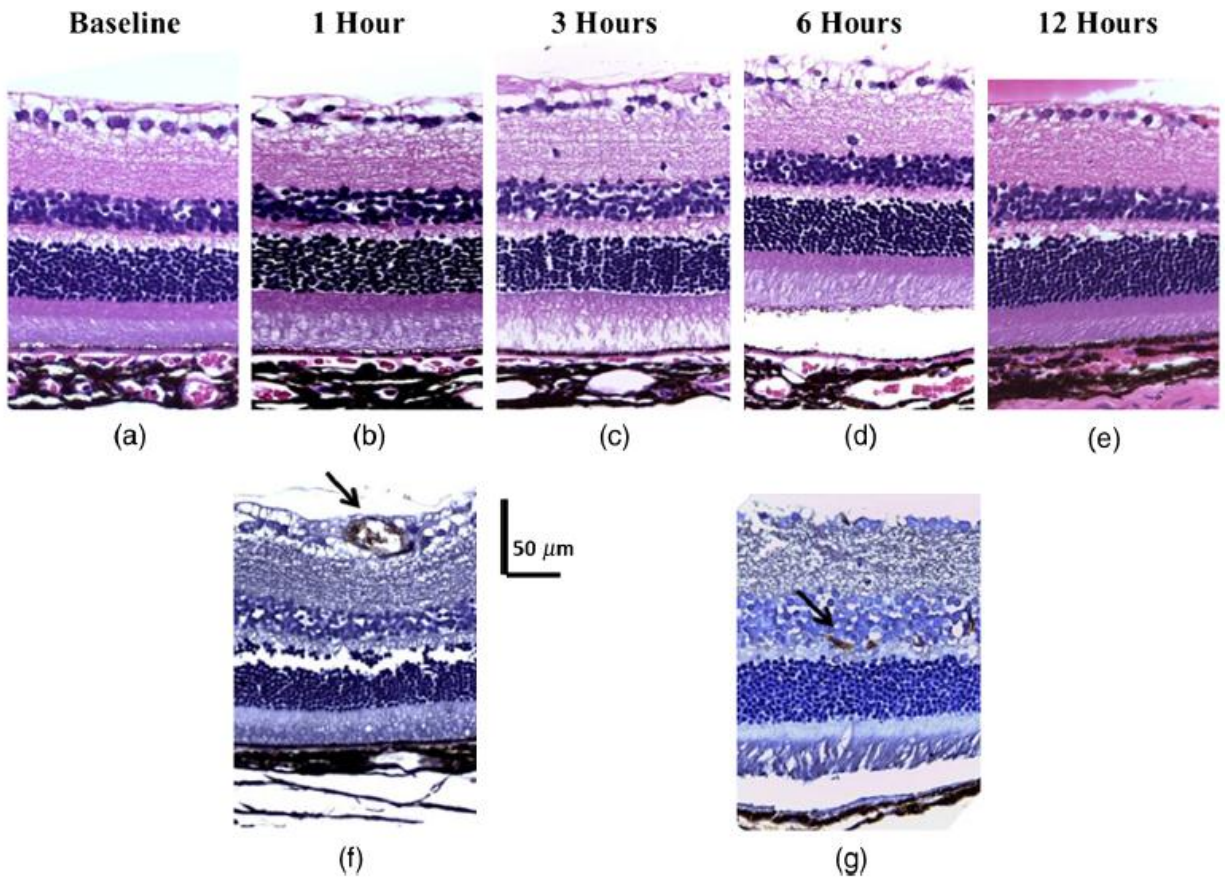

Fig. 5.7 From (a) to (e): representative H&E histology images acquired at baseline and 1, 3 6, 12 hours post $NaIO_3$ injection respectively. (f) and (g): stained histology images acquired at 1 and 6 hours post injection respectively. Figure adopted and reprinted from reference [11].

5.3 DOMAG Images and ONH Blood Flow Rate Estimation

As mentioned in the last chapter, two more $NaIO_3$ injected rats, named F and G, were used to study the ONH blood flow from baseline to one week post injection. Fig. 5.8 contains representative 2D morphological OCT, DOCT, OMAG and DOMAG images acquired using circular scan mode at baseline for rat F.

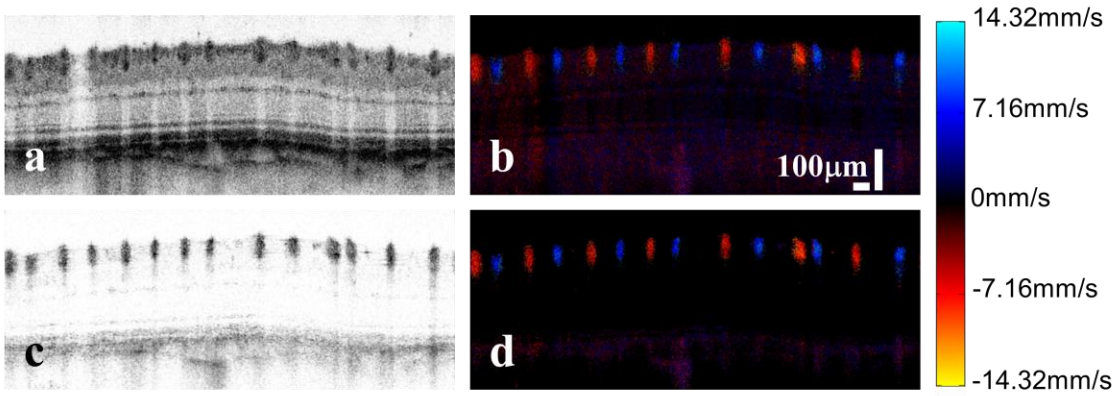

Fig. 5.8 Representative 2D (a) morphological OCT, (b) DOCT, (c) OMAG and (d) DOMAG images acquired using circular scan mode at baseline for rat F. The estimated axial velocity parallel to the imaging beam of each pixel is indicated by different colors, with blue as positive (towards imaging beam) and red as negative (away from imaging beam). The magnitude of axial velocity is shown by the color bar at the right.

By comparing Fig. 5.8 (a) and (c), the OMAG method shows its capability of effectively removing the static reflections from regions in the retinal tissue, which contain no blood flow. The INL, IPL, ONL and part of the PR layer in the OCT image are all filtered in the OMAG image. The blood vessels, mainly ONH and choroid, are expected to be preserved because they contain blood flows. In addition, part of the outer segment is still visible in the OMAG image, which might be attributed to the fact that this layer located relatively deeper in the retina such that multiple light scattering and speckle noise were more significant. In addition, cellular motion in the PR layer may also result in the OS being preserved in the OMAG image. Similarly, the comparison between Fig. 5.8 (b) and (d) shows that while the DOCT image suffers from structural phase noise, the DOMAG image only preserves the Doppler OCT signal in the ONH and the choroid. Each ONH vessel in Fig 5.8 (d) is very clear and distinguishable with the axial velocity information well defined. On the other hand, the axial velocity information of the choroid is somewhat random and insufficient for quantitative analysis, which might possibly due to the much smaller sizes of choroidal vessels than the ONH; most choroidal vessels were nearly perpendicular to the imaging beam such that their flow velocities were hardly detectable; the choroid located deep under the retina where multiple light reflection played an essential role to disturb the phase information.

Figs. 5.9 and 5.10 contain representative 2D morphological OCT and DOMAG images acquired using circular scan mode at baseline and 1, 3, 6, 12, 24, 72, 168 hours post injection for rat F and G.

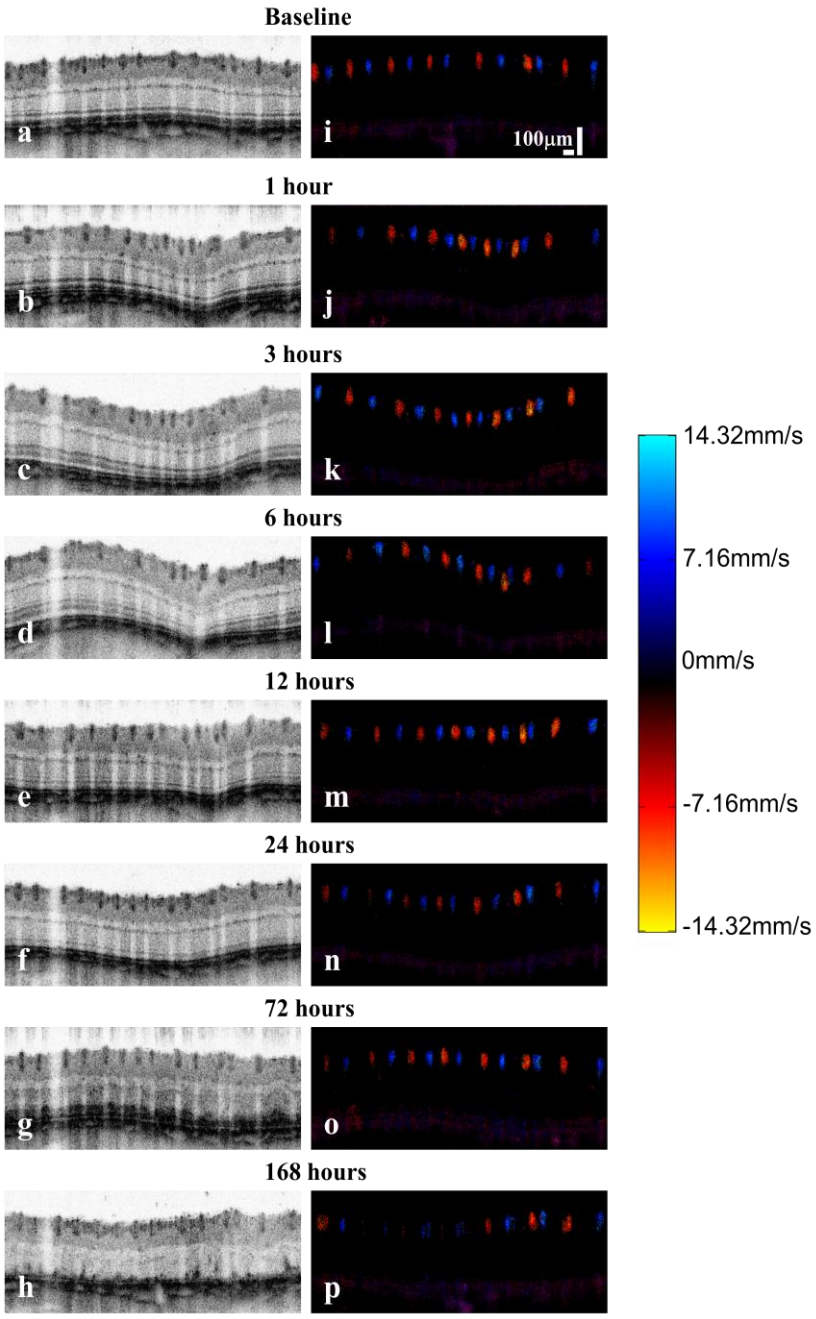

Fig. 5.9 Representative 2D images acquired using circular scan mode for rat F. From (a) to (h): morphological OCT images acquired at baseline and 1, 3 6, 12, 24, 72, 168 hours post $NaIO_3$ injection respectively. From (i) to (p): DOMAG images acquired at baseline and 1, 3 6, 12, 24, 72, 168 hours post $NaIO_3$ injection respectively.

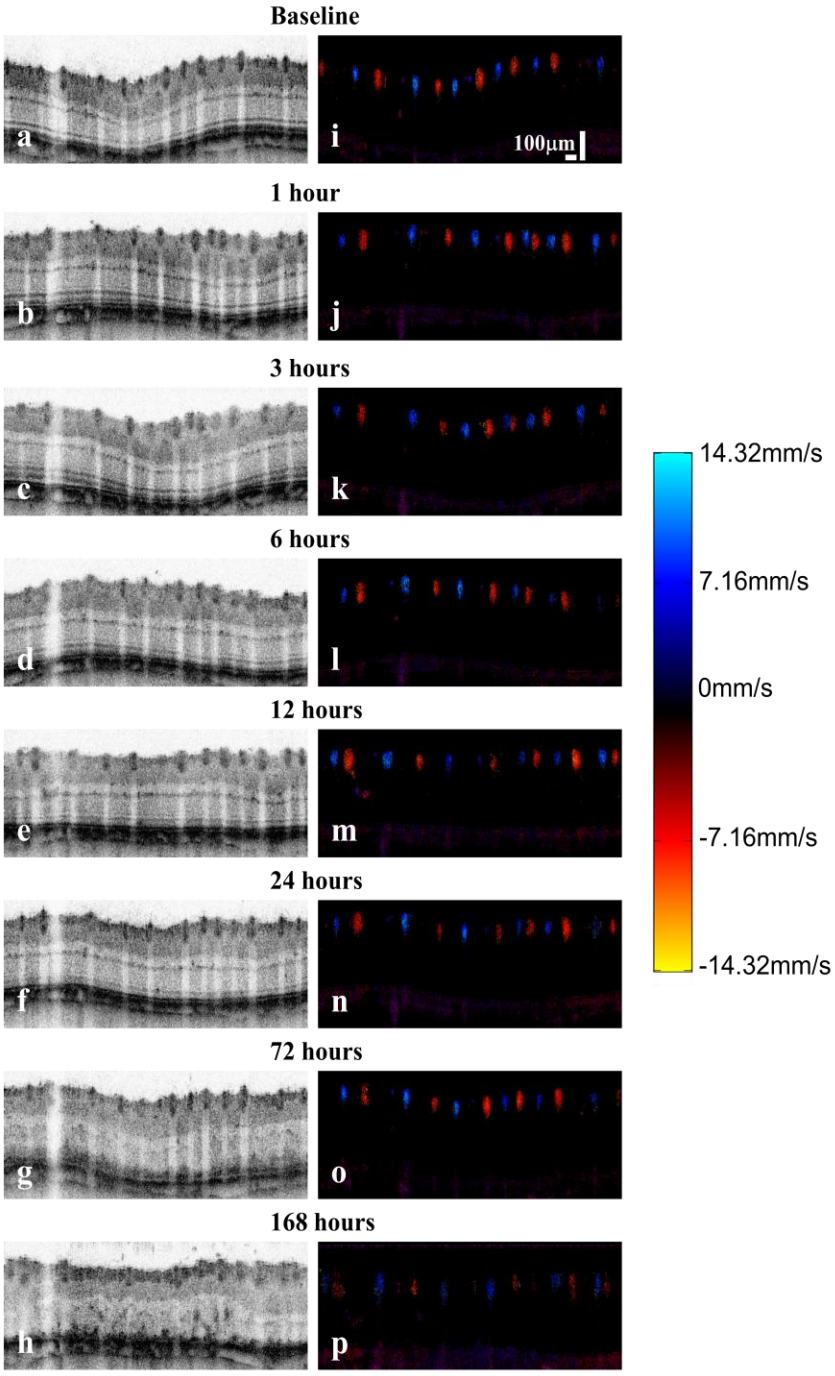

Fig. 5.10 Representative 2D images acquired using circular scan mode for rat G. From (a) to (h): morphological OCT images acquired at baseline and 1, 3 6, 12, 24, 72, 168 hours post $NaIO_3$ injection respectively. From (i) to (p): DOMAG images acquired at baseline and 1, 3 6, 12, 24, 72, 168 hours post $NaIO_3$ injection respectively.

Rat F was identified to have 14 ONH vessels in total with 7 arteries and 7 veins, while Rat G was identified to have 12 ONH vessels in total with 6 arteries and 6 veins, as shown in Fig 5.11.

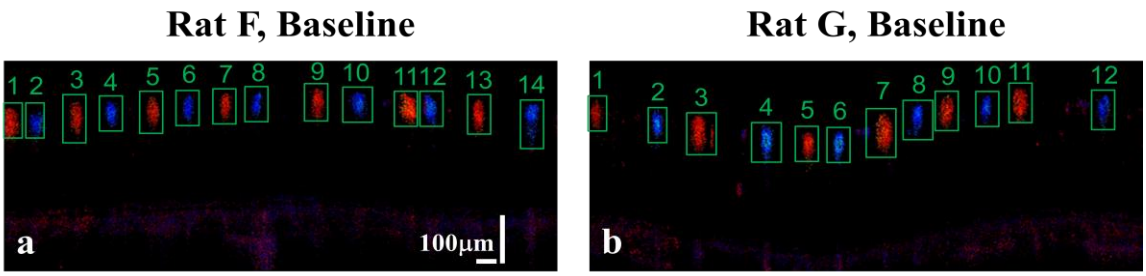

Fig. 5.11 Representative 2D images acquired using circular scan mode for (a) rat F and (b) rat G. Rat F was identified to have 14 ONH vessels in total with 7 arteries and 7 veins, while Rat G was identified to have 12 ONH vessels in total with 6 arteries and 6 veins.

As mentioned in chapter 4, in order to reduce the error due to motion artifacts and speckle noise, 200 repetitive circular B-scan images were acquired around the same location in the retina for signal averaging. The estimated axial velocities, Doppler angles, vessel diameters, absolute velocities and flow rate for all ONH vessels of rat F and G at baseline are summarized in Tables 5.1 and 5.2 respectively. The ONH vessel diameters, absolute velocities and flow rates calculated for our two rats show high consistency with are with that of the rats reported in reference [9], except some particular vessels had slightly larger flow rates. This is expected since they used Brown Norway rats, different from the Long Evans rats we used and the retinal morphology and blood perfusion for the two rat species are fairly different. The estimated flow rate of all ONH vessels for both rats at all time points are summarized in Tables 5.3 and 5.4. Figs. 5.12 and 5.13 are graphical presentations of the flow rate of every ONH vessel, including all veins and arteries, for rat F and G respectively, while Fig. 5.14 is graphical presentation of the averaged flow rates of all ONH vessels for rat F and G. The errors of axial velocities and vessels diameters displayed in Tables 5.1 and 5.2 were estimated based on the fluctuations of those two quantities over the 200 circular B-scans in each set of image acquisition, which were originated from pulsatile blood flow, motion artifacts and speckle noise. Together with the uncertainty of Doppler angle, the errors of flow rates were estimated and summarized in Tables 5.3- 5.4. They are also visualized as error bars in Figs. 5.12-5.13, while in Fig. 5.14, each error bar is the standard deviation of flow rates of all ONH vessels in every time point for each rat.

Vessel No.	Axial Velocity (mm/s)	Doppler Angle	Vessel Diameter (μm)	Absolute Velocity (mm/s)	Flow Rate (μL/min)
1	4.4±0.3	70.4±1.0	60.5±4.8	13.1±1.2	2.26±0.41
2	4.4±0.4	67.5±1.0	59.6±4.2	11.4±1.3	1.90±0.34
3	3.6±0.2	68.3±1.0	61.2±4.4	9.6±0.8	1.70±0.28
4	5.3±0.5	62.3±1.0	51.6±2.3	11.4±1.0	1.44±0.19
5	3.9±0.3	64.5±1.0	57.3±3.2	9.1±0.8	1.40±0.20
6	4.5±0.7	55.8±1.0	51.9±3.2	7.9±1.3	1.01±0.20
7	3.9±0.3	59.9±1.0	51.5±3.2	7.8±0.6	0.98±0.14
8	4.4±0.4	61.4±1.0	51.6±3.3	9.2±1.0	1.16±0.19
9	3.7±0.3	59.7±1.0	59.0±5.0	7.3±0.7	1.19±0.23
10	5.0±0.3	62.7±1.0	59.4±1.7	10.8±0.8	1.80±0.16
11	5.4±0.4	58.2±1.0	65.6±2.8	10.3±0.8	2.09±0.24
12	5.5±0.4	65.7±1.0	55.1±1.4	13.4±1.1	1.91±0.19
13	4.8±0.4	56.1±1.0	57.7±3.1	8.6±0.8	1.35±0.19
14	4.0±0.6	67.5±1.0	59.6±6.7	10.4±1.5	1.74±0.47

Table 5.1 Estimated axial velocities, Doppler angles, vessel diameters, absolute velocities and flow rates for all ONH vessels of rat F imaged at baseline.

Vessel No.	Axial Velocity (mm/s)	Doppler Angle	Vessel Diameter (μm)	Absolute Velocity (mm/s)	Flow Rate (μL/min)
1	3.1±0.4	70.0±1.0	51.8±2.1	9.0±1.1	1.14±0.17
2	5.3±0.8	51.8±1.0	59.1±5.2	8.5±1.3	1.40±0.13
3	4.4±0.3	61.2±1.0	70.5±2.9	9.1±0.6	2.14±0.23
4	6.7±0.3	63.5±1.0	71.1±1.1	15.1±0.8	3.60±0.22
5	4.7±0.3	58.0±1.0	70.2±3.4	8.9±0.6	2.06±0.13
6	6.6±0.3	54.4±1.0	59.6±2.4	11.3±0.5	1.89±0.18
7	5.1±0.3	50.0±1.0	87.1±0.3	7.9±0.4	2.82±0.16
8	5.2±0.6	55.4±1.0	65.9±0.8	9.2±1.0	1.89±0.21
9	4.7±0.3	54.6±1.0	71.8±1.6	8.0±0.5	1.95±0.15
10	5.0±0.6	51.8±1.0	53.2±4.5	8.0±1.0	1.07±0.12
11	4.2±0.2	48.8±1.0	70.7±1.1	6.4±0.4	1.51±0.10
12	4.5±0.7	54.9±1.0	69.3±6.7	7.8±1.2	1.77±0.21

Table 5.2 Estimated axial velocities, Doppler angles, vessel diameters, absolute velocities and flow rates for all ONH vessels of rat G imaged at baseline.

Vessel No.	Baseline	1 h	3 h	6 h	12 h	24 h	72 h	168 h
1	2.26±0.41	0.36±0.13	0.96±0.17	0.79±0.22	0.97±0.19	1.12±0.29	0.54±0.13	1.19±0.39
2	1.90±0.34	1.24±0.10	1.04±0.14	1.30±0.22	1.06±0.24	1.17±0.34	0.72±0.32	1.44±0.59
3	1.70±0.28	2.71±0.38	0.88±0.26	1.23±0.21	0.72±0.16	0.29±0.09	0.50±0.14	0.08±0.03
4	1.44±0.19	4.09±0.28	1.33±0.19	1.55±0.23	0.78±0.16	2.35±0.44	1.25±0.21	0.30±0.26
5	1.40±0.20	2.94±0.33	0.53±0.13	1.16±0.17	0.71±0.14	0.54±0.14	0.65±0.12	0.05±0.23
6	1.01±0.20	3.37±0.18	1.14±0.12	0.85±0.11	1.40±0.17	0.64±0.21	1.00±0.11	0.30±0.26
7	0.98±0.14	3.07±0.19	0.70±0.10	1.42±0.23	0.99±0.15	0.90±0.19	1.00±0.13	0.02±0.13
8	1.16±0.19	2.38±0.20	0.90±0.09	0.66±0.14	0.99±0.20	0.74±0.24	0.72±0.08	0.24±0.22
9	1.19±0.23	3.38±0.21	1.26±0.14	0.97±0.24	1.13±0.12	1.40±0.23	1.14±0.14	0.94±0.16
10	1.80±0.16	2.47±0.22	0.94±0.31	0.09±0.08	0.83±0.22	0.88±0.29	0.81±0.10	0.77±0.36
11	2.09±0.24	2.99±0.19	1.40±0.29	0.89±0.28	1.16±0.12	2.32±0.24	1.13±0.09	1.59±0.25
12	1.91±0.19	3.27±0.33	0.96±0.28	0.77±0.34	0.84±0.14	1.38±0.15	0.88±0.20	0.98±0.18
13	1.35±0.19	2.30±0.19	1.92±0.21	0.31±0.16	1.53±0.11	1.45±0.22	0.88±0.14	1.13±0.30
14	1.74±0.47	0.90±0.21	1.34±0.19	1.55±0.48	1.30±0.16	0.86±0.22	0.47±0.21	0.68±0.36

Table 5.3 Estimated flow rates for all ONH vessels of rat F imaged at baseline and 1, 3 6, 12, 24, 72, 168 hours post $NaIO_3$ injection respectively.

Vessel No.	Baseline	1 h	3 h	6 h	12 h	24 h	72 h	168 h
1	1.14±0.17	2.08±0.29	1.12±0.16	0.06±0.07	1.10±0.20	1.07±0.16	2.82±0.45	1.39±0.56
2	1.40±0.13	2.35±0.22	1.93±0.20	0.46±0.33	1.58±0.21	0.91±0.30	3.24±0.37	0.59±0.33
3	2.14±0.23	1.31±0.18	2.19±0.20	0.99±0.43	2.77±0.34	2.87±0.37	0.96±0.25	1.74±0.41
4	3.60±0.22	2.18±0.22	1.96±0.24	1.74±0.56	1.78±0.32	2.50±0.34	1.40±0.22	1.56±0.16
5	2.06±0.13	2.36±0.28	0.97±0.18	0.55±0.33	0.97±0.18	0.64±0.14	1.65±0.27	1.25±0.18
6	1.89±0.18	1.46±0.27	1.50±0.14	0.72±0.46	1.19±0.30	1.88±0.27	1.13±0.31	0.80±0.24
7	2.82±0.16	1.83±0.24	2.79±0.13	0.89±0.60	0.19±0.15	0.64±0.16	1.51±0.25	0.69±0.32
8	1.89±0.21	1.79±0.23	1.04±0.12	0.50±0.35	0.72±0.20	0.66±0.20	0.77±0.34	1.86±0.22
9	1.95±0.15	2.79±0.33	0.55±0.10	0.78±0.44	0.75±0.17	1.14±0.26	1.75±0.33	2.03±0.32
10	1.07±0.12	1.68±0.37	1.15±0.23	0.36±0.21	1.15±0.25	0.93±0.31	1.12±0.47	2.46±0.33
11	1.51±0.10	0.59±0.12	2.06±0.13	0.70±0.51	2.64±0.33	1.94±0.27	0.24±0.11	2.22±0.68
12	1.77±0.21	1.50±0.24	2.11±0.29	0.19±0.18	2.01±0.20	1.44±0.46	1.26±0.32	2.03±0.40

Table 5.4 Estimated flow rates for all ONH vessels of rat G imaged at baseline and 1, 3 6, 12, 24, 72, 168 hours post $NaIO_3$ injection respectively.

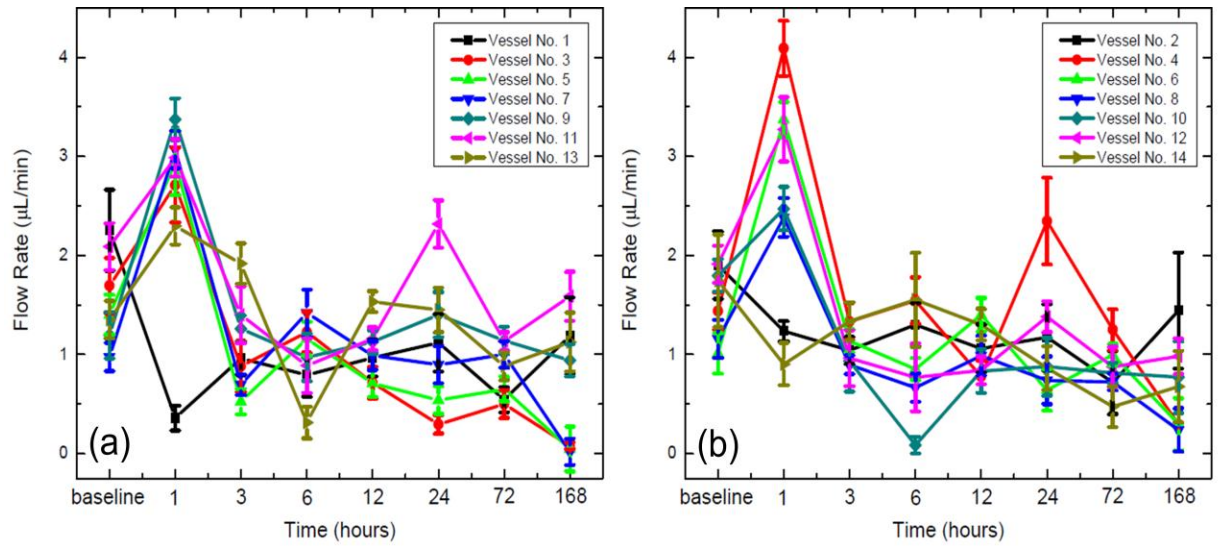

Fig. 5.12 Plot of flow rates of ONH vessel (a) no. 1, 3, 5, 7, 9, 11, 13 (all veins) and (b) no. 2, 4, 6, 8, 10, 12, 14 (all arteries) of rat F versus different post injection time points.

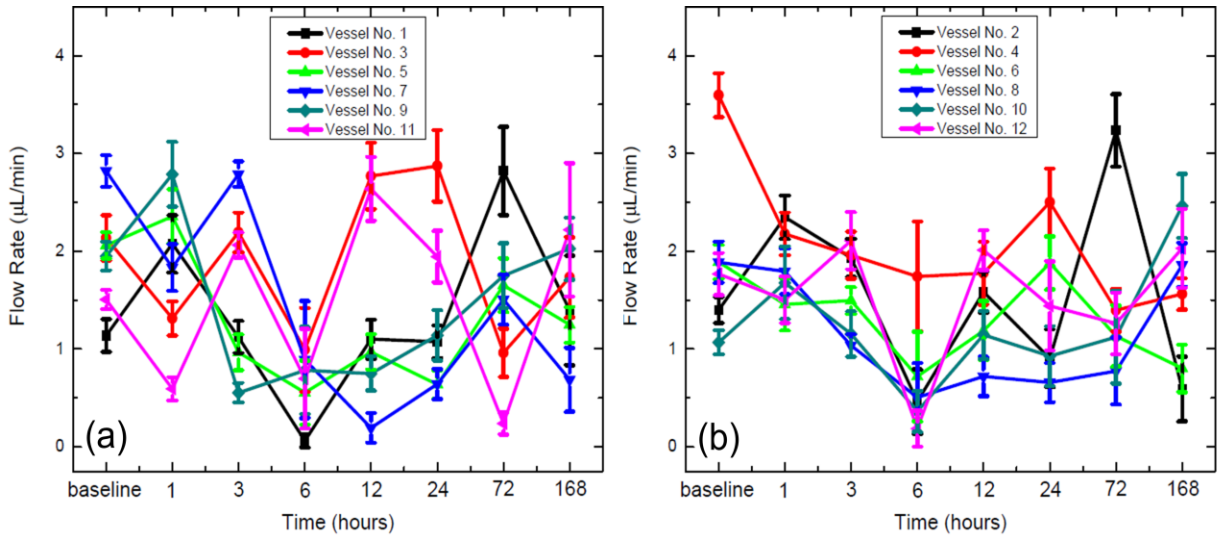

Fig. 5.13 Plot of flow rates of ONH vessel (a) no. 1, 3, 5, 7, 9, 11 (all veins) and (b) no. 2, 4, 6, 8, 10, 12 (all arteries) of rat G versus different post injection time points.

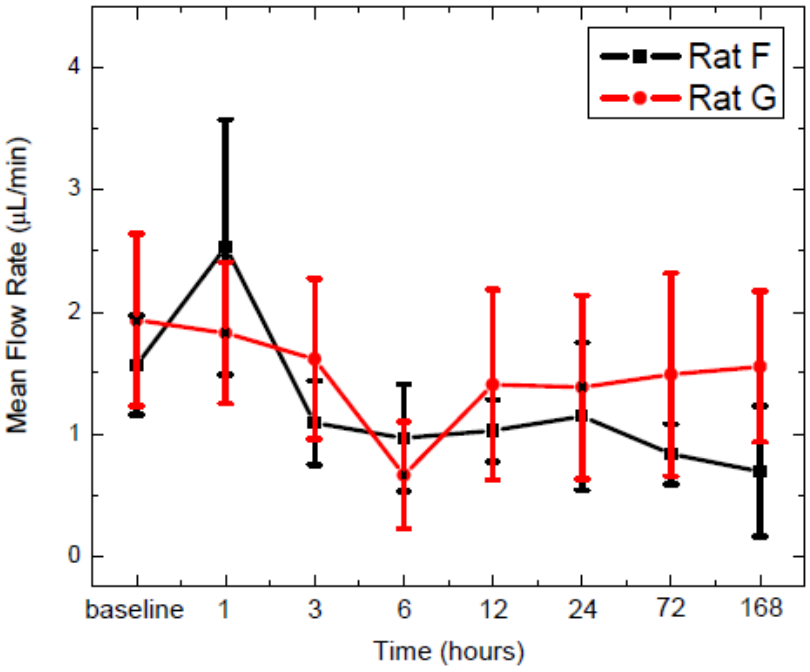

Fig. 5.14 Plot of mean flow rates of all ONH vessels for rat F (black line) and G (red line) versus different post injection time points.

5.4 Discussions

5.4.1 Morphological Results

The structural changes in the IS and OS layers observed in the morphological OCT and histological images correlated very well. The continuous morphing of the low and highly reflective bands in the photoreceptor IS/OS layer suggested re-arrangement of the photoreceptors inner and outer segments. In addition, there was a slight increase in overall IS/OS layer thickness at 1 hour post injection as compared to the baseline image, which suggested some cell swelling. Such hypothesis was confirmed by the H&E histology in Fig. 5.7(b), which shows RPE and PR cell swelling as well as re-arrangement of the photoreceptor OS. The structural change of OS in this study was consistent with the observation using electron microscopy in reference [36]. The temporal increase of reflectance in OS at the early hours post injection might be attributed to the separation of OS from the RPE, as well as damaged RPE which leaded to disc accumulation of cellular debris. The LRL appeared between the RPE and the OS at the early hours post injection was most likely due to fluid accumulation. It was an early response to the $NaIO_3$ toxicity which

leaded to disruption of the blood-retina barrier and detachment of the PR from the RPE layer. It was also a possible cause of the rearrangement of OS structure. From the images of 12 hours post injection, not only the LRL disappeared but there was also a significant reflectance drop of the whole PR layer due to clearance of highly reflective materials.

The time of appearance and disappearance as well as thickness of the LRL varied among rats, since each animal had a different metabolism. For all the rats used in this study, only rats D and E were observed to have the LRL appeared at 1 hour post injection, while the others did not or had the LRL showed up at 3 hour post injection. Nevertheless, it was very likely there is a strong correlation between the LRL and the degeneration of the PR. From the observation of all the morphological OCT images above, at the time point where the LRL started to appear, the PR also morphed significantly.

5.4.2 Blood Flow Results

For the quantitative retinal blood flow analysis, the estimated flow rates shown in Table 5.3-5.4 and Figs. 5.12-5.14 are within 0.02-4.09mL/min, which are reasonable values compared with the results in reference [9]. From Fig. 5.12, rat F had all vessels except vessel no. 1, 2 and 14 which showed a sudden increase of flow rate at 1 hour post injection followed by decrease at hour 3 and 6. In a long term basis up to 168 hours, there was an overall flow rate consistent decrease of all ONH vessels. From Fig. 5.13, the flow rate of all vessels rat G did not show consistent decreasing throughout the 168 hours. However, it is noticeable that all vessels had their flow rates drop to minimum at hour 6. To the best of our knowledge, this thesis is the first work that measures the ONH flow rates of $NaIO_3$ injected rats. Fig. 5.14 shows the averaged flow rate of all vessels at different time points for both rats. The flow rate drop at hour 6 in both rats suggests there was possibly a correlation between the ONH flow and the degeneration of the PR as well as the appearance of the LRL.

Nevertheless, the flow rate calculation was subjected to some uncertainties. Some error bars displayed in Figs. 5.12 and 5.14 are quite large, which suggests significant fluctuation of blood flow due to pusatile and motion artifact. Several issues were also encountered in Doppler angle estimation. It is noticeable that the long time used for image acquisition with the vigorous bulk motion of the rat could lead to the inaccurate angle measurement. With a 47 kHz A-line rate,

the acquisition time for the linear scan mode (1000 A-scans times 1000 B-scans) took 26.6s, while for circular scan mode (3000 A-scans times 200 B-scans), it took 16.0s. Although repetitive B-scans and averaging could somewhat suppress the error due to motion artifact in the axial velocity calculation of circular scan images, the 3D image composed from linear B-scans still suffered from the artifact even with the help of image registration. Consider the imaging beam diameter of the circular scan was set to be half of the transverse range in the linear scan, the Doppler angle of each vessel was estimated at the midpoint between the ONH center and the position where the vessel reached the edge of the 3D image. However, it took ~10s for the switching between the linear and circular scan mode. It was possible the rat's eye had already moved to another position during the switching (or even worse, had the eye and all vessels tilted to a different angle), which resulted in a difference of the scanning centre between the linear and circular mode. Consider all vessels were actually continuous curving channels instead of straight lines, it was highly possible that erroneous Doppler angles were measured at positions off from the circular scan trace. Furthermore, the FOV was assumed to be ~1.77mm for linear scan mode and ~2.8mm for circular scan mode respectively. Those estimations were based on reference [10]. Practically each individual rat had a different eye diameter and lens focal length such that the FOV could vary between different rats. This leaded to an inaccurate estimation not only the Doppler angle but also the vessel size.

Similar problem also appeared among different imaging time points. Not only the $NaIO_3$ toxicity caused changes of PR thickness and possibly orientation of each ONH vessel, but also for every hour the rat was anesthetized, there was no guarantee that the imaging position being the same. Our experimental condition was very different from the glaucoma study in reference [9], where the rat was keep in the same position with the whole IOP changing process. In our study, it was required to take the rat off from the anesthesia system after each imaging time point passed. Finally, disruption of ONH vessels was observed in 168 hours post injection, as shown in Figs. 5.9h and 5.10h. Although this caused an apparent decrease in axial velocity in Figs. 5.9p and 5.10p, the shapes of the vessels were also significantly deformed in which they were hard to be identified. This also caused an imprecision in vessel area and flow rate estimation. For improvement in Doppler angle estimation, it is suggested that the OCT system is assisted with a fundus camera to help aligning the retina at the same imaging position every hour the rat is anesthetized. Imaging protocols have to be modified to reduce the image acquisition time and

switching time between scanning modes, or use different approaches to do the Doppler angle and flow rate measurement. More precise models have to be considered to make more precise estimations of FOVs.

5.5 Conclusions

In summary, the work in this thesis shows the early effect of $NaIO_3$ on the morphology of the rat outer retina using high speed SD-OCT, as well as up to our best knowledge, quantitative analysis of the effect of $NaIO_3$ on the ONH blood flow of rats for the first time. 7 Long Evans rats were injected with $NaIO_3$ and imaged by a SD-OCT system. 5 rats were used to study outer retinal degeneration at baseline and 1, 3, 6, 12 hours post injection; 2 rats were used to study the ONH blood flow at baseline and 1, 3, 6, 12, 24, 72, 168 hours post injection. Morphological OCT images showed changes of reflectance and thickness of the photoreceptor IS and OS. The formation of a low reflective layer between the photoreceptor OS and the RPE was observed in all tested animals. Such layer appeared as early as 1 hour, increased in thickness after 6 hours and disappeared by 12 hours post $NaIO_3$ injection. The dynamics of LRL suggested that it was most likely originated from fluid accumulation. Comparison between morphological OCT and histology images show photoreceptor OS cell swelling at hour 1, detachment of the OS from the RPE by hour 3 and breaking of the blood-retina barrier with significant fluid accumulation by hour 6 post $NaIO_3$ injection. The morphology study shows SD-OCT as an effective tool to carry out non-invasive, in-vivo studies of disease or drug induced retinal degeneration in ophthalmic research.

Estimation of flow rate on each ONH vessel was done by measurements of the Doppler angle, vessel size and the axial velocity. The ONH flow rates of rat F showed a consistent decrease over the 168 hours of study, while rat G did not show such trend. Both rats had flow rates of most ONH vessels dropped at hour 6, which indicated there was possibly a correlation between the ONH flow and the degeneration of the PR as well as the appearance of the LRL. The flow rate estimation was subjected some uncertainties such as deviation of Doppler angle due to bulk motion artifact of animal. Nevertheless, this study has demonstrated that the capability of SD-OCT to quantify retinal blood flow and suggest a possible linkage between $NaIO_3$ toxicity and ONH flow rates which requires further verifications.

Appendix A

Accuracy Test of Doppler OCT Algorithm Using a Phantom Flow System

In order to test DOCT's reliability of quantitatively analyzing fluid flow, a phantom flow system using titanium dioxide (TiO_2) solution as the fluid was built and the flow was imaged by the SD-OCT system. The experimental methods, comparison of flow rate estimation using DOCT phase-resolved algorithm with expected value and discussions are provided below.

A.1 Methods

A mixture of TiO_2 powder with water was used as the phantom fluid to simulate retinal blood flow. The schematic of the phantom flow setup is shown in Fig. A.1. The syringe was filled with TiO_2 solution and mounted on a mechanical pump. It was connected to a glass capillary with diameter $d = 0.3\text{mm}$ through a plastic hose. The TiO_2 solution was given a pressure by the pump to move through the syringe and the capillary with a flow rate of $30\,\mu\text{L/min}$. The sample probe was mounted on a semi-circle arm to acquire B-scan images of the capillary at 7 different angles $\theta = 0^\circ, -10^\circ, -20^\circ, -30^\circ, 10^\circ, 20^\circ, 30^\circ$ with respect to the vertical.

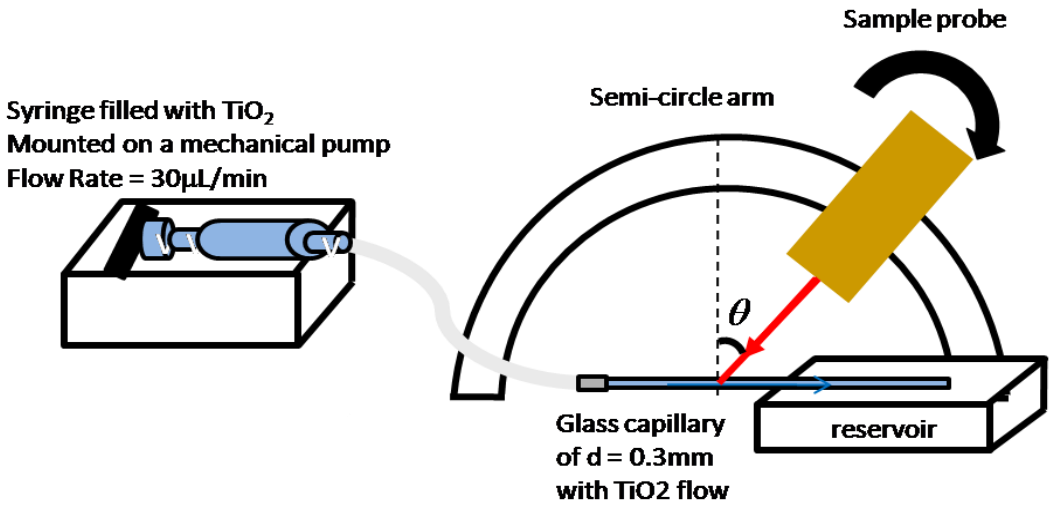

Fig. A.1 A schematic showing the phantom flow system.

The flow rate F of TiO_2 solution through the capillary is defined as

$$F = \sum_{i,j} v(i,j)\Delta A(i,j) \tag{A.1}$$

At the position (i, j), $v(i, j)$ is the absolute velocity with its direction parallel to the capillary, $\Delta A(i, j)$ is the capillary cross-sectional area with its normal parallel to the flow direction. Refer to Fig. A.2, in a DOCT image, what could be directed measured by the phase-resolved method were the axial velocity $v_z(i, j)$ parallel to the imaging beam and the cross-sectional area $\Delta A'(i, j)$ with its normal perpendicular to the imaging beam. The beam entering the capillary was refracted to an angle θ', which could be obtained by applying Snell's law $n_{\text{air}} \sin\theta = n_{\text{TiO}_2} \sin\theta'$, with $n_{\text{air}} = 1$ and $n_{\text{TiO}_2} = 1.33$.

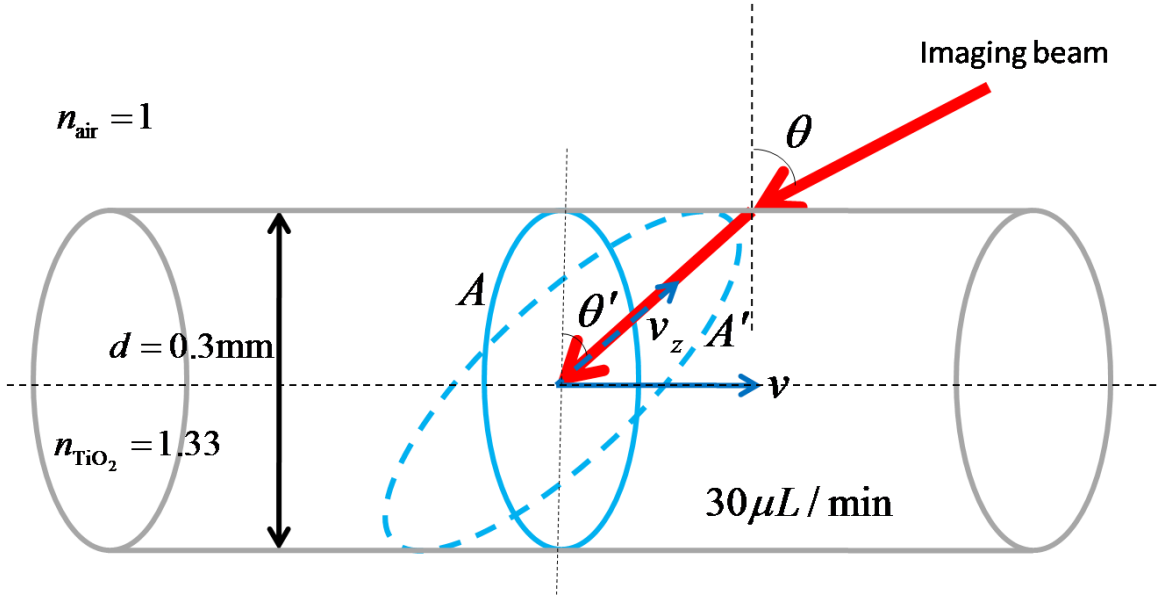

Fig. A.2 A schematic showing the flow rate estimation of TiO_2 solution through the glass capillary.

The parameters above can be related as $v(i, j) = v_z(i, j) / \sin\theta'$ and $\Delta A(i, j) = \Delta A'(i, j)\cos\theta'$. Therefore the flow rate can be expressed as

$$F = \sum_{i,j} v_z(i,j)\Delta A'(i,j)\cot\theta' \tag{4.2}$$

A.2 Results and Discussions

Fig. A.3 shows the color DOCT B-scan images of the capillary at different angles. The negative and positive values of θ were corresponding to the axial velocity v_z pointing away and towards the incident imaging beam respectively. The axial velocities, visualized by different colors shown in Fig. A.3 (a)-(g) with the values given by the color bar at the right, were consistent with our expectation, in which the red and blue color represented the flow moving away and towards to the imaging probe respectively. As the magnitude of v_z increased with θ, the color also became brighter (from dark red to yellow or from dark blue to cyan). For $\theta = 0^\circ$, the color was dimmest, which was also expected as the measurable v_z approached zero.

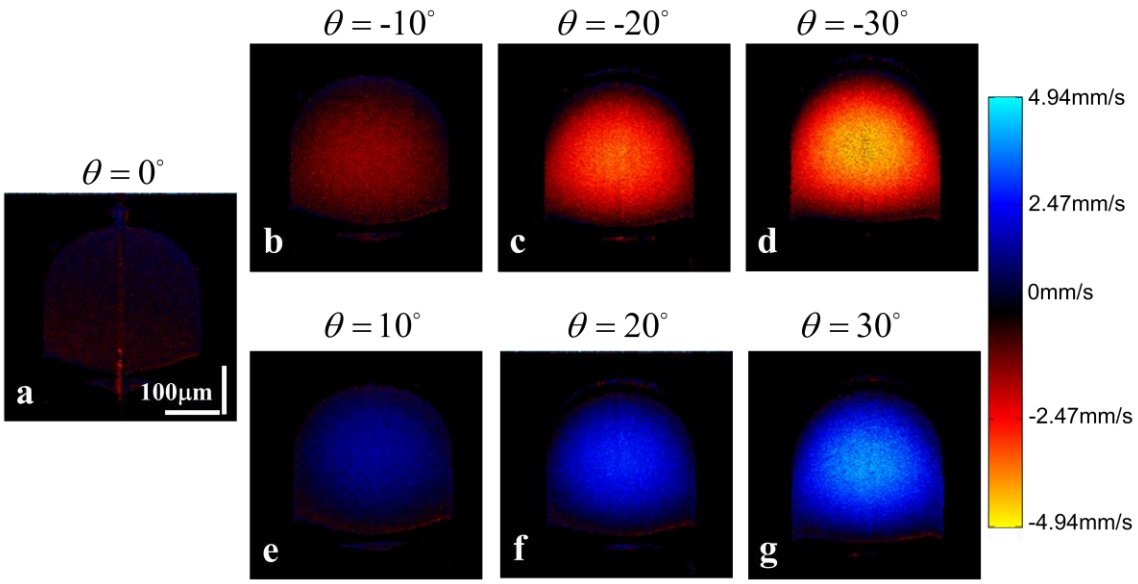

Fig. A.3 Color DOCT B-scan images of the capillary with TiO_2 flow acquired at different imaging angles. (a)-(g) are corresponding to angle $\theta = 0^\circ, -10^\circ, -20^\circ, -30^\circ, 10^\circ, 20^\circ, 30^\circ$ respectively.

The results of TiO_2 flow rate estimation at different angles are summarized in Table A.1. All values were close to the expected value of $30\,\mu L/min$. They were all slightly underestimated, which could be attributed to several reasons. The syringe might move slightly when being pushed by the mechanical pump in which the actual flow rate was possibly smaller than $30\,\mu L/min$. In addition, the wall thickness of the glass capillary and the background phase noise were neglected, which might result in a deviation of θ' and flow rate calculation. Nevertheless,

to conclude, this phantom flow test showed the DOCT phase resolved algorithm was working reasonably well and appropriate to be applied for quantitative analysis of retinal blood flow.

Incident Angle θ (°)	Refracted Angle θ' (°)	Flow Rate (μL/min)
-30	-22.1	28.4
-20	-14.9	29.7
-10	-7.5	24.1
10	7.5	29.8
20	14.9	24.4
30	22.1	26.2

Table A.1 Estimated flow rates of TiO_2 through the glass capillary at different imaging angles.

Copyright Permissions

Part of Chapter 5 (sections 5.1, 5.2, 5.4.1) is based on the following published paper:

S. Hariri, M. C. Tam, D. Lee, D. Hileeto, A. A. Moayed, and K. Bizheva, "*Non-invasive imaging of the early effect of sodium iodate toxicity in a rat model of outer retina degeneration with SD-OCT*", J. Biomed. Opt. 18(2), 026017 (2013)

Necessary permissions have been obtained permitting me to include my published work in this thesis. Contact e-mail address: mc2tam@uwaterloo.ca

Bibliography

[1] Wolfgang Drexler and James G. Fujimoto (Eds.), "*Optical Coherence Tomography: Technology and Applications*", Springer-Verlag Berlin Heidelberg (2008)

[2] D. Huang, E. A. Swanson, C. P. Lin, J. S. Schuman, W. G. Stinson, W. Chang, M. R. Hee, T. Flotte, K. Gregory and C. A. Puliafito, "*Optical coherence tomography*", Science 254(5035), 1178–1181 (1991)

[3] M. Wojtkowski, "*High-speed optical coherence tomography: basics and applications*", Appl. Opt. 49, 16 (2010)

[4] S. Schmitz-Valckenberg, M. Fleckenstein, A. P. Göbel, T. C. Hohman and F. G. Holz, "*Optical coherence tomography and autofluorescence findings in areas with geographic atrophy due to age-related macular degeneration*", Invest. Ophthalmol. Vis. Sci. 52(1), 1–6 (2011)

[5] A. J. Witkin, L. N. Vuong, V. J. Srinivasan, I. Gorczynska, E. Reichel, C. R. Baumal, A. H. Rogers, J. S. Schuman, J. G. Fujimoto and J. S. Duker, "*High-speed ultrahigh resolution optical coherence tomography before and after ranibizumab for age-related macular degeneration*", Ophthalmology 116(5), 956–963 (2009)

[6] Y. Chen, L. N. Vuong, J. Liu, J. Ho, V. J. Srinivasan, I. Gorczynska, A. J. Witkin, J. S. Duker, J. Schuman and J. G. Fujimoto, "*Three-dimensional ultrahigh resolution optical coherence tomography imaging of age-related macular degeneration*", Opt. Express 17(5), 4046–4060 (2009)

[7] T. Fukuchi, K. Takahashi, K. Shou and M. Matsumura, "*Optical coherence tomography (OCT) findings in normal retina and laser-induced choroidal neovascularization in rats*", Graefes Arch. Clin. Exp. Ophthalmol. 239(1), 41–46 (2001)

[8] G. Wollstein, L. A. Paunescu, T. H. Ko, J. G. Fujimoto, A. Kowalevicz, I. Hartl, S. Beaton, H. Ishikawa, C. Mattox, O. Singh, J. Duker, W. Drexler and J. S. Schuman, "*Ultrahigh-Resolution Optical Coherence Tomography in Glaucoma*", Ophthalmology 112(2), 229–237 (2005)

[9] Z. Zhi, W. Cepurna, E. Johnson, T. Shen, J. Morrison and R. K. Wang, "*Volumetric and quantitative imaging of retinal blood flow in rats with optical microangiography*", Biomed. Opt. Express2(3), 579-591 (2011)

[10] S. Hariri, A. A. Moayed, V. Choh, and K. Bizheva, "*In vivo assessment of thickness and*

reflectivity in a rat outer retinal degeneration model with ultrahigh resolution optical coherence tomography", Invest. Ophthalmol. Vis. Sci. 53(4), 1982–1989 (2012)

[11] S. Hariri, M. C. Tam, D. Lee, D. Hileeto, A. A. Moayed, and K. Bizheva, "*Non-invasive imaging of the early effect of sodium iodate toxicity in a rat model of outer retina degeneration with SD-OCT*", J. Biomed. Opt. 18(2), 026017 (2013)

[12] M. Wojtkowski, V. J. Srinivasan, T. H. Ko, J. G. Fujimoto, A. Kowalczyk and J. S. Duker, "*Ultrahigh-resolution, high-speed, Fourier domain optical coherence tomography and methods for dispersion compensation*", Opt. Express 12(11), 2404-2422 (2004)

[13] G. Liu, W. Qi, L Yu and Z. Chen, "*Real-time bulk-motion-correction free Doppler variance optical coherence tomography for choroidal capillary vasculature imaging*", Opt. Express 19(4), 3657-3666 (2011)

[14] Z. Chen, T. E. Milner, D. Dave and J. S. Nelson, "*Optical Doppler tomographic imaging of fluid flow velocity in highly scattering media*", Opt. Lett. 22(1), 64-66 (1997)

[15] J. A. Izatt, M. D. Kulkarni and S. Yazdanfar, "*In vivo bidirectional color Doppler flow imaging of picoliter blood volumes using optical coherence tomography*", Opt. Lett. 22(18), 1439-1441(1997)

[16] Y. Zhao, Z. Chen, C. Saxer, Q. Shen, S. Xiang, J. F. de Boer and J. S. Nelson, "*Doppler standard deviation imaging for clinical monitoring of in vivo human skin blood flow*", Opt. Lett. 25(18), 1358-1360 (2000)

[17] R. A. Leitgeb, L. Schmetterer, W. Drexler, A. F. Fercher, R. J. Zawadzki and T. Bajraszewski "*Real-time assessment of retinal blood flow with ultrafast acquisition by color Doppler Fourier domain optical coherence tomography*", Opt. Express 11(23), 3116-3121(2003)

[18] C. Kasai, K. Namekawa, A. Koyano and R. Omoto, "*Real-time two-dimensional blood flow imaging using an autocorrelation technique*", IEEE Transactions on Sonics and Ultrasonics 32(3), 458-464 (1985)

[19] L. An and R. K. Wang, "*In vivo volumetric imaging of vascular perfusion within human retina and choroids with optical micro-angiography*", Opt. Express 16(15), 11438-11452 (2008)

[20] C. Kolbitsch, T. Schmoll and R. A. Leitgeb, "*Histogram-based filtering for quantitative 3D retinal angiography*", J. Biophoton. 2, No. 6–7, 416–425 (2009)

[21] Z. Zhi, W. O. Cepurna, E. C. Johnson, J. C. Morrison and R. K. Wang, "*Impact of intraocular pressure on changes of blood flow in the retina, choroid, and optic nerve head in rats investigated by optical microangiography*", Opt. Express 3(9), 2220-2233(2012)

[22] Y. Jia, L. An and R. K. Wang, "*Label-free and highly sensitive optical imaging of detailed microcirculation within meninges and cortex in mice with the cranium left intact*", J. Biomed. Opt. 15(3), 030510 (2010)

[23] S. Makita, Y. Hong, M. Yamanari, T. Yatagai and Y. Yasuno, "*Optical coherence angiography*",Opt. Express 14(17), 7821-7840 (2006)

[24] R. K. Wang, S. L. Jacques, Z. Ma, S. Hurst, S. R. Hanson and A. Gruber, "*Three dimensional optical angiography*", Opt. Express 15(7), 4083-4097 (2007)

[25] R K Wang, "*Directional blood flow imaging in volumetric optical microangiography achieved by digital frequency modulation*", Opt. Lett. 33(16), 1878-1880 (2008)

[26] Z. Yuan, Z. C. Luo, H. G. Ren, C. W. Du and Y. Pan, "*A digital frequency ramping method for enhancing Doppler flow imaging in Fourier domain optical coherence tomography*", Opt. Express 17(5), 3951-3963 (2009)

[27] Y. K. Tao, A. M. Davis and J. A. Izatt, "*Single-pass volumetric bidirectional blood flowimaging spectral domain optical coherence tomography using a modified Hilbert transform*", Opt. Express 16(16), 12350-12361 (2008)

[28] Y. K. Tao, K. M. Kennedy and J. A. Izatt, "*Velocity-resolved 3D retinal microvessel imaging using single-pass flow imaging spectral domain optical coherence tomography*", Opt. Express 17(5), 4177-4188 (2009)

[29] R. K. Wang and L. An, "*Doppler optical micro-angiography for volumetric imaging of vascular perfusion in vivo*", Opt. Express 17(11), 8926-8940 (2009)

[30] Y. Wen, M. Klein, D. C. Hood and D. G. Birch, "*Relationships among multifocal electroretinogram amplitude, visual field sensitivity, and SD-OCT receptor layer thicknesses in patients with retinitis pigmentosa*", Invest. Ophthalmol. Vis. Sci. 53(2), 833–840 (2012)

[31] A. Sorsby, "*Experimental pigmentary degeneration of the retina by sodium iodate*", Br J Ophthalmol 25(2), 58–62 (1941)

[32] Y. H. Yoon and M. F. Marmor, "*Retinal pigment epithelium adhesion to Bruch's membrane is weakened by hemicholinium-3 and sodium iodate*", Ophthalmic Res. 25(6), 386–392 (1993)

[33] W. S. Redfern, S. Storey, K. Tse, Q. Hussain, K. P. Maung, J.-P. Valentin, G. Ahmed, A. Bigley, D. Heathcote and J. S. McKay, "*Evaluation of a convenient method of assessing rodent visual function in safety pharmacology studies: Effects of sodium iodate on visual acuity and retinal morphology in albino and pigmented rats and mice*", Journal of Pharmacological and Toxicological Methods 63(1), 102–114 (2011)

[34] V. Enzmann, B. W. Row, Y. Yamauchi, L. Kheirandish, D. Gozal, H. J. Kaplan and M. A. McCall, "*Behavioral and anatomical abnormalities in a sodium iodate-induced model of retinal pigment epithelium degeneration*", Exp. Eye Res. 82(3), 441–448 (2006)

[35] L. Hosoda, E. Adachi-Usami, A. Mizota, T. Hanawa and T. Kimura, "*Early effects of sodium iodate injection on ERG in mice*", Acta Ophthalmol (Copenh) 71(5), 616–622 (1993)

[36] M. Tanaka, S. Machida, K. Ohtaka, Y. Tazawa, and J. Nitta, "*Third-order neuronal responses contribute to shaping the negative electroretinogram in sodium iodate-treated rats*", Curr. Eye Res. 30(6), 443–453 (2005)

[37] A. Machalińska, W. Lubiński, P. Kłos, M. Kawa, B. Baumert, K. Penkala, R. Grzegrzółka, D. Karczewicz, B. Wiszniewska and B. Machaliński, "*Sodium iodate selectively injuries the posterior pole of the retina in a dose-dependent manner: morphological and electrophysiological study*", Neurochem. Res. 35(11), 1819–1827 (2010)

[38] Y. Murakami, Y. Ikeda, Y. Yonemitsu, M. Onimaru, K. Nakagawa, R. Kohno, M. Miyazaki, T. Hisatomi, M. Nakamura, T. Yabe, M. Hasegawa, T. Ishibashi and K. Sueishi, "*Inhibition of nuclear translocation of apoptosis-inducing factor is an essential mechanism of the neuroprotective activity of pigment epithelium-derived factor in a rat model of retinal degeneration*", Am. J. Pathol. 173(5), 1326–1338 (2008)

[39] T. Kohno, T. Miki, K. Shiraki and M. Matsushita, "*Choriocapillary changes and hyperfluorescence on indocyanine green angiography*", Graefes Arch. Clin. Exp. Ophthalmol. 236(2), 122–131 (1998)

[40] A. A. Moayed, S. Hariri, V. Choh and K. Bizheva, "*In vivo imaging of intrinsic optical signals in chicken retina with functional optical coherence tomography*", Opt. Lett. 36(23), 4575-4577 (2011)

[41] A. Mizota and E. Adachi-Usami, "*Functional recovery of retina after sodium iodate injection in mice*", Vision Res 37(14), 1859–1865 (1997)

[42] O. Textorius, E. Welinder, and S. E. Nilsson, "*Combined effects of DL-alpha-aminoadipic acid with sodium iodate, ethyl alcohol, or light stimulation on the ERG c-wave and on the standing potential of albino rabbit eyes*", Doc Ophthalmol 60(4), 393–400 (1985)

[43] Y. Wang, B. A. Bower, J. A. Izatt, O. Tan and D. Huang, "*Retinal blood flow measurement by circumpapillary Fourier domain Doppler optical coherence tomography*", J. Biomed. Opt. 13(6), 064003 (2008)

[44] R. F. Spaide and C. A. Curcio, "*Anatomical correlates to the bands seen in the outer retina by optical coherence tomography: literature review and model*", Retina (Philadelphia, Pa.) 31(8), 1609–1619 (2011)